

Research Paper

Diurnal waves forced by horizontal convergence of near-surface winds on Mars

David Hinson^{a,*}, John Wilson^b^a Carl Sagan Center, SETI Institute, Mountain View, CA 94043, USA^b Space Science and Astrobiology Division, NASA Ames Research Center, Moffett Field, CA 94035, USA

ARTICLE INFO

Keywords:

Mars, atmosphere
Atmospheres, dynamics
Meteorology

ABSTRACT

Boundary-layer winds near steeply sloped topography excite a distinct type of atmospheric wave. Basic properties of the waves were determined through analysis of 7 Mars years of temperature profiles from the Mars Climate Sounder on Mars Reconnaissance Orbiter. A more complete understanding of the waves was derived from a simulation with the NASA Ames Mars General Circulation Model. This type of wave appears in the tropics in the vicinity of conspicuous surface features, such as large volcanoes and the rim of Isidis Planitia. The amplitude is typically 5–10 K, the vertical wavelength is about 40 km, the zonal wavelength is about 1400 km, and the zonal phase speed relative to the surface is about 25 m s⁻¹. The wave forcing comes from horizontal convergence of the near-surface winds, which generates a daily surge in the vertical winds. These convergence zones were not previously recognized as an important source of atmospheric waves on Mars. Strong forcing occurs only within a limited range of local time, producing wave packets (diurnal pulses) rather than steady oscillations. Waves are present throughout the year and their properties vary with season. Near the solstices, the wave amplitude is largest in the tropics of the summer hemisphere, where the convergence zones are stronger than in the winter hemisphere. The diurnal-mean zonal winds, which vary with latitude and season, control the direction of propagation of the predominant waves through filtering by critical levels.

1. Introduction

As context for the results reported here, we include a summary of atmospheric waves observed previously at low latitudes on Mars. These can be divided into three categories defined by the horizontal direction of propagation. *Sub-planetary-scale inertia-gravity waves* can propagate in any direction, as determined by the source of excitation. Waves in the other two categories are global-scale solutions to Laplace's tidal equations (Andrews et al., 1987). *Kelvin waves* can propagate only eastward; the meridional structure is Gaussian and centered on the equator. *Planetary-scale inertia-gravity waves* can propagate eastward or westward; they have a more complex meridional structure than the Kelvin wave. The discussion that follows is organized by the spatial scale of the observed waves, beginning with the global-scale thermal tides.

The general circulation of the atmosphere of Mars includes large-amplitude thermal tides, which cause daily, global oscillations in pressure, temperature, and wind (Zurek et al., 1992; Barnes et al., 2017). One class of tides consists of planetary-scale inertia-gravity waves that

travel westward with the Sun. These *migrating tides* arise from solar heating and radiative cooling of aerosols within the atmosphere, as well as from solar heating of the surface and subsequent heat transfer to the atmosphere. Both the diurnal and the semidiurnal migrating tides have been observed by a variety of instruments (Barnes et al., 2017), including the Mars Climate Sounder (MCS) on Mars Reconnaissance Orbiter (MRO) (Kleinböhl et al., 2013; Wu et al., 2017; Forbes et al., 2020) and the Fourier spectrometer on the ExoMars Trace Gas Orbiter (Fan et al., 2022b). In addition to those two modes, the Emirates Mars InfraRed Spectrometer (EMIRS) has also detected the terdiurnal migrating tide (Fan et al., 2022a).

Tides with shorter periods, most notably 6 and 4 h, have been detected in surface pressure measurements by Curiosity (Wilson et al., 2017) and Perseverance (Sánchez-Lavega et al., 2023). The amplitude of both modes varies strongly with season (Sánchez-Lavega et al., 2023, Fig. 5), consistent with the behavior of the quaddiurnal and hexadiurnal migrating tides in simulations with a Mars General Circulation Model (MGCM) (Wilson et al., 2017, Fig. 1). These modes have not yet been observed from orbit.

* Corresponding author.

E-mail addresses: dhinson@seti.org (D. Hinson), robert.j.wilson@nasa.gov (J. Wilson).

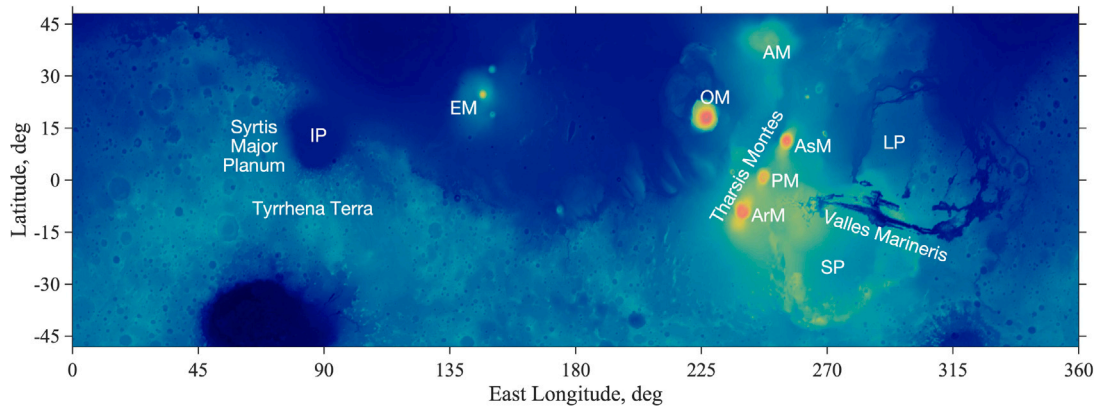


Fig. 1. Map of surface elevation (Smith et al., 2001) annotated to show the locations of surface features discussed in this paper. These include Isidis Planitia (IP), Elysium Mons (EM), Olympus Mons (OM), Arsia Mons (ArM), Pavonis Mons (PM), Ascraeus Mons (AsM), Alba Mons (AM), Solis Planum (SP), and Lunae Planum (LP).

Another class of tides is not Sun synchronous. These *nonmigrating tides* arise from zonal modulation of both the migrating tides and the solar forcing. The former comes from zonal variations of topography, while the latter comes from zonal variations in surface albedo and the distribution of clouds and dust. The best-known nonmigrating tide on Mars is the diurnal Kelvin wave with zonal wavenumber $s = 1$ (DE1, where E denotes eastward). Its equivalent barotropic vertical structure results in large variations in surface pressure and geopotential height (Zurek, 1988; Wilson and Hamilton, 1996; Wilson, 2000; Hinson et al., 2008). MCS temperature measurements have greatly expanded the inventory of nonmigrating tides known to be present on Mars. For example, three diurnal Kelvin waves (DE1, DE2, and DE3) have been identified through analysis of MCS data (Guzewich et al., 2012; Wu et al., 2015; Forbes et al., 2020). In addition to the diurnal Kelvin waves, other nonmigrating tides were identified in each of those studies, including D0 and SE1 (Guzewich et al., 2012); DW2, DW3, and SW1 (Wu et al., 2015); and SE1, S0, and SW1 (Forbes et al., 2020). (S denotes semidiurnal.)

Sub-planetary-scale waves are generated by processes such as orographic forcing and convection; they differ from the tides not only in spatial scale but also in frequency and direction of propagation. Most of what is known about these waves comes from two types of remote sensing. One is based on measurements of brightness temperature. Through analysis of MCS observations at emission angles of $\sim 0^\circ$ (nadir) and $\sim 70^\circ$ (off-nadir), Heavens et al. (2020, 2022b) derived a comprehensive global record of wave activity spanning more than 6 Mars years. The nadir observations (acquired only in MY28¹) are sensitive to waves with horizontal wavelengths λ_h of 10–30 km and vertical wavelengths λ_z of at least 50 km. The off-nadir observations (acquired routinely subsequent to MY28) are sensitive to larger λ_h (10–80 km) and smaller λ_z (5–30 km), with greatest sensitivity to waves with $\lambda_h / \lambda_z \approx 2$. In both nadir and off-nadir data, the period of the waves that can be observed is well under 1 h, which corresponds to the high end of the gravity-wave frequency spectrum. (The maximum frequency of a gravity wave is the buoyancy frequency N , about 10^{-2} s^{-1} .) This method of analysis has also been applied to nadir observations of brightness temperature by the Thermal Emission Spectrometer on Mars Global Surveyor (Heavens et al., 2022a).

Another type of remote sensing has been used to explore a different part of the wave spectrum — with smaller λ_z than the thermal tides and larger λ_h than the high-frequency gravity waves. These waves are identified through the oscillations they produce in individual temperature profiles. Waves with large λ_z , such as the thermal tides described above, are removed from the data through use of a filter. The properties

of the remaining inertia-gravity waves are then determined from the filtered profiles. This technique has been applied to limb observations by a variety of instruments (Creasey et al., 2006; Ando et al., 2012; Wright, 2012; Tellmann et al., 2013; Starichenko et al., 2021). The upper bound on λ_z imposed by the filter ranges from 10 to 30 km in the studies cited here. The value of λ_h is poorly constrained by this type of observation, but it is generally assumed to be several hundred kilometers or more.

The results reported here are an extension of preliminary work by Wilson and Hinson (2021), who analyzed MCS data — both brightness temperatures and retrieved temperature profiles — in search of zonal variations that are indicative of waves. In addition to characterizing the planetary-scale thermal tides, they found a type of wave that had not been observed previously by MCS or any other instrument. Its vertical and horizontal wavelengths, about 40 km and 1400 km, respectively, are outside the ranges covered by the investigations described above — smaller λ_h than the thermal tides, larger λ_h than the high-frequency gravity waves, and larger λ_z than the inertia-gravity waves in the limb profiles. This paper provides a more complete characterization of this new type of wave, derived in equal parts from analysis of MCS temperature profiles and from a simulation by the NASA Ames MGCM. Most importantly, we have identified the forcing mechanism, characterized the diurnal cycle of wave activity, and determined how the waves are influenced by the diurnal-mean zonal winds.

It is convenient to adopt a descriptive name for the waves considered here. As shown in Section 4.2, the waves are a consequence of horizontal convergence of near-surface winds. Although the topographic circulation follows a regular diurnal cycle, the wave forcing varies strongly with time of day, resulting in wave packets rather than steady oscillations. We therefore refer to this type of wave as a diurnal wave packet (DWP); the acronym is used here mainly to avoid ambiguity.

These convergence zones are part of the boundary-layer circulation induced by sloping topography. This is the first detailed investigation of their capacity to excite atmospheric waves. The results reported here are complementary to previous studies, which focused primarily on the impact of the topographic circulations on the depth of the convective boundary layer and the diurnal variations of surface pressure (Tyler and Barnes, 2013, 2015; Wilson et al., 2017; Hinson et al., 2019).

The paper is organized as follows. Section 2.1 discusses the MCS temperature profiles and their distribution in longitude, latitude, and local time. Section 2.2 describes the NASA Ames MGCM and how it was configured in this investigation. Section 3 explains the method of analysis. Section 4 presents the results, including the general properties of the waves (Section 4.1), their diurnal cycle (Sections 4.1 and 4.2), the forcing mechanism (Section 4.2), and wave filtering by critical levels (Section 4.3). The results are summarized in Section 5. Fig. 1 shows the locations of surface features discussed in Sections 4 and 5.

¹ Mars year 1 (MY01) began on 11 April 1955 (Clancy et al., 2000), at the vernal equinox in the northern hemisphere ($L_s = 0^\circ$).

2. Data and model

2.1. Mars climate sounder

MRO circles Mars in a sun-synchronous polar orbit that crosses the equator at local times of ~ 3 h on the nightside and ~ 15 h on the dayside (Zurek and Smrekar, 2007). Successive equator crossings at each local time are separated by $\sim 27^\circ$ of longitude. MCS monitors the atmosphere methodically, with each orbit yielding nearly continuous pole-to-pole coverage at two local times. See McCleese et al. (2007) for a description of the MCS instrument and its operations. The MCS retrieval algorithm is explained by Kleinböhl et al. (2009, 2011).

This investigation is based on MCS temperature profiles acquired over a span of 7 Mars years (MY29–35). (MCS also retrieves profiles of water-ice opacity, which are discussed briefly in Section 4.1.) We used Version 5 of the Derived Data Records stored at the Atmospheres Node of the NASA Planetary Data System (<https://pds-atmospheres.nmsu.edu>). MCS can sound the atmosphere at the limb anywhere along a 270° arc of azimuth. Most of the profiles used here were retrieved from in-track observations, with the instrument pointed at an azimuth of $\sim 180^\circ$ (forward) or $\sim 0^\circ$ (aft). We also used profiles retrieved from both cross-track observations (azimuths of $\sim 90^\circ$ and $\sim 270^\circ$) and off-track observations (azimuths intermediate to the other observations). However, cross-track and off-track profiles were used only if the local time of the retrieved profile is within 2 h of the in-track (sub-spacecraft) local time. Though relatively few in number, the cross-track and off-track profiles improve the quality of the results by filling problematic gaps in the spatial coverage of the in-track profiles.

Some gaps in spatial coverage arise from spacecraft operations. For example, MCS does not observe the atmosphere when MRO is communicating with the Curiosity rover, owing to concerns about UHF interference (David Kass, personal communication, February 2022). This produces large, systematic gaps in the MCS observations in all data acquired after $L_s = 168^\circ$ of MY31. The gap is apparent in Fig. 2 at longitudes of about 120 – 150° E, where in-track observations are absent from the southern tropics on the nightside (Fig. 2A) and from the northern tropics on the dayside (Fig. 2B). This type of gap is filled effectively by cross-track and off-track profiles from orbits not affected by communications with Curiosity.

There is also a smaller gap in the nighttime profiles centered on the equator at 300° E (Fig. 2A). It is present during the aphelion season of all years. MCS retrievals of water-ice opacity suggest that it results from a local cloud whose opacity is sufficient to limit the vertical range of atmospheric sounding. This sort of gap is present in all types of observations (in-, off-, and cross-track), as shown in Fig. 2A. Its impact on the investigation is discussed in Section 3.

2.2. NASA Ames MGCM

We obtained additional information about the waves and the general circulation of the atmosphere from a simulation by the NASA Ames MGCM. The general configuration of the model is described by Bertrand et al. (2020). The specific version used here employs the simple representation of water ice clouds described in Kleinböhl et al. (2013) and Wilson and Guzewich (2014), rather than the more complex microphysics described in Haberle et al. (2019), which follows the details of ice deposition onto a spectrum of dust particles. The model physics is otherwise the same as in the NASA Ames Legacy MGCM (Haberle et al., 2019). The model has a finite-volume cubed-sphere (FV3) dynamical core, which can perform simulations at a horizontal resolution as small as ~ 7 km (Wilson et al., 2017), expanding the scope of high-resolution simulations from the local nest of a mesoscale model to global scale.

In the simulation used here, each face of the cube has 48 by 48 elements (C48) and the nominal horizontal resolution is ~ 110 km. There were 36 vertical levels that transition from terrain-following

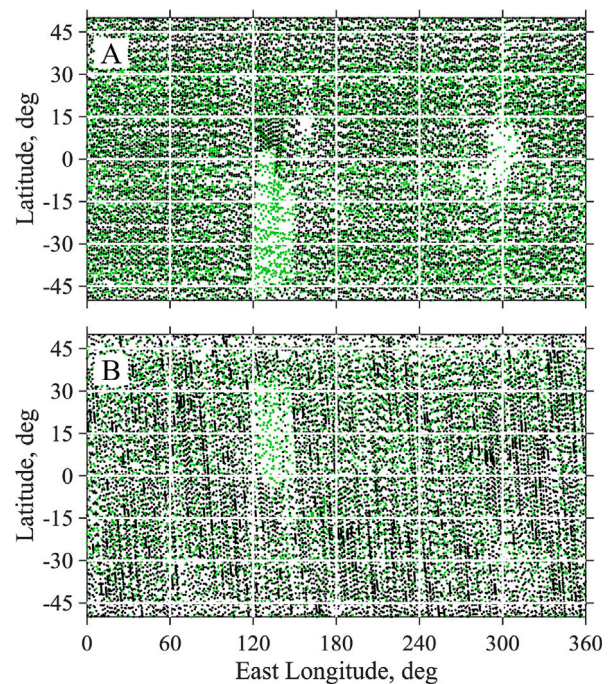


Fig. 2. Spatial distribution of MCS profiles at the 9-Pa pressure level in (A) nighttime observations from $L_s = 81$ – 99° of MY33 and (B) dayside observations from $L_s = 261$ – 279° of MY33. Black dots denote in-track observations; green dots denote cross-track and off-track observations. The set of profiles in A includes 12,335 in-track, 5905 right cross-track, 5319 left cross-track, and 148 off-track observations. The set of profiles in B includes 11,835 in-track, 2810 right cross-track, 2925 left cross-track, and 157 off-track observations. (For interpretation of the references to color in this figure legend, the reader is referred to the web version of this article.)

sigma coordinates near the surface to constant pressure at high altitudes. The horizontal distribution and seasonal evolution of the dust column opacity were constrained to follow the MY30 dust climatology of Montabone et al. (2015), but the vertical distribution of dust evolved freely in response to advection and sedimentation, as in Bertrand et al. (2020). The spatial distributions of both water vapor and cloud ice were determined entirely by advection, sedimentation, condensation, and sublimation in the simulated temperature and wind fields. The clouds were radiatively active.

Output from the full simulation is prohibitively large; a condensed version of the results was used in this study. The following fields are needed to characterize the state of the atmosphere: temperature, pressure, and the zonal, meridional, and vertical wind speeds. Each field was sampled at intervals of 2° in both latitude and longitude on each of the 36 vertical levels. These results were stored sequentially at uniform intervals of time on the prime meridian (24 per sol). In addition, surface pressure and surface temperature were sampled 24 times per sol on the same 2° by 2° horizontal grid. Hence, each sol of output consists of 4-D arrays of temperature, pressure, and winds, and 3-D arrays of surface pressure and surface temperature. The data volume was reduced further by computing 5-sol averages of the single-sol arrays. The end result is a 32-GB file that consists of 134, non-overlapping, 5-sol averages spanning 1 year. A subset of this file is publicly available (doi.org/10.5281/zenodo.7407335); it contains information sufficient to reconstruct Figs. 8–15, which show results from the MGCM simulation.

The simulation was used to determine the zonal phase speed of the waves, to characterize the diurnal cycle of wave activity, to identify the forcing mechanism, and to investigate the effect of the diurnal-mean zonal winds on wave propagation. As we show in Section 4, the waves in the simulation compare favorably with those observed by MCS, which confirms that C48 horizontal resolution is sufficient for

this investigation. This conclusion is supported by comparisons with selected results from a C192 simulation, as discussed in Section 4.2. Convergence zones associated with small-scale topography are not resolved by the C48 simulation, but that limitation does not affect our conclusions.

3. Method of analysis

The wave-induced temperature variations T' are modeled as

$$T'(\lambda, \phi, p, t_U) = A(\phi, p) \cos[s\lambda - \omega t_U - \delta(\phi, p)]. \quad (1)$$

Here, s is the zonal wavenumber, λ is east longitude, ω is the frequency, and t_U is universal time. The amplitude A and phase δ depend on latitude ϕ and pressure p . For example, δ varies with ϕ for a wave traveling other than due east or due west. In the sign convention used here, s is positive and the sign of ω determines the direction of propagation.

It is convenient to define a dimensionless frequency $\sigma = \omega/\Omega$, where Ω is the rotation rate of Mars. When T' is expressed in terms of the local true solar time t_L , Eq. (1) becomes

$$T'(\lambda, \phi, p, t_L) = A(\phi, p) \cos[(s + \sigma)\lambda - \sigma\Omega t_L - \delta(\phi, p)], \quad (2)$$

where

$$\Omega t_L = \Omega t_U + \lambda. \quad (3)$$

When the wave structure is viewed at fixed local time, the zonal wavenumber is $m = s + \sigma$. The fixed-local-time perspective is used for all figures in Section 4, and the zonal structure is therefore expressed in terms of m .

When viewed at fixed t_U , as in Eq. (1), the group velocity is parallel to the wavefronts (Andrews et al., 1987). When viewed at fixed t_L , as in Eq. (2), the wavefronts have a different orientation; the vertical structure is the same as in Eq. (1) but the zonal wavenumber has changed from s to m . However, the change in orientation is small for the waves considered here, where $m \approx 15$, $|\sigma| \approx 2$, and $m \approx s$. The wavefronts therefore remain closely aligned with the group velocity even when the wave structure is viewed at fixed t_L .

The temperatures retrieved by MCS were sorted into bins of size 18° in L_s and 6° in latitude, with a separate set of bins for each pressure level, local time (3 or 15 h), and Mars year. Henceforth, subsets of data are identified by the values of L_s and latitude at the center of the bin. The data in each bin were conditioned, first by removing the seasonal trend, and then by averaging samples within 4° windows of longitude; all data samples were weighted equally regardless of their formal uncertainties. Least-squares analysis was applied to the conditioned data to solve for zonal harmonics at $m = 1$ –30. Each harmonic takes the form

$$T'_m = A_m \cos[m\lambda - \gamma_m], \quad (4)$$

where γ_m combines the last two terms in the argument of the cosine in Eq. (2). Independent solutions for A_m and γ_m were derived from the subset of data at each L_s , latitude, pressure, local time, and Mars year.

The resulting database of wave properties spans 7 Mars years (MY29–35). To provide some flexibility in displaying the results, least-squares analysis was performed for bins centered every 9° of L_s and every 3° of latitude (78°S – 78°N). The database has entries at two local times and 34 vertical levels equally spaced in log-pressure (0.1–370 Pa). The interval between pressure levels is ~ 2.5 km, half the vertical resolution of the MCS profiles. Oversampling ensures that the information in the profiles is fully utilized.

Fig. 3A illustrates characteristics of the sub-planetary-scale waves observed by MCS in the wavenumber range $m = 8$ –24; the reason for choosing this range is explained below. These results are from the northern summer solstice ($L_s = 90^\circ$). The latitude is 21°N , the local time is 3 h, and the pressure is 18 Pa. An independent solution for

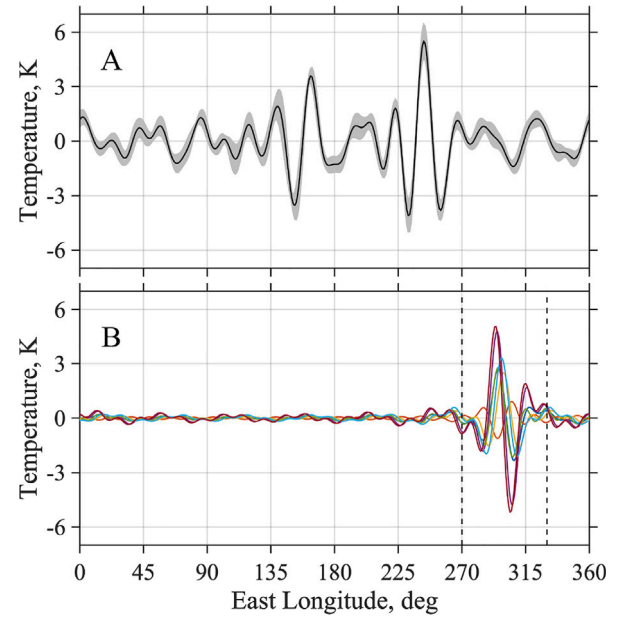


Fig. 3. (A) The average value (black line) and standard deviation (gray shading) of the wave-induced temperature variations observed by MCS in 7 consecutive years at the same season ($L_s = 90^\circ$), latitude (21°N), local time (3 h), and pressure (18 Pa). The wavenumber range is $m = 8$ –24. (B) Results from a sensitivity study where data were removed from a 20° longitude band centered at 300°E . The difference between the new fit and the previous solution is shown for each of the 7 years. Dashed lines mark the boundaries of the region where the solution is degraded. (For interpretation of the references to color in this figure legend, the reader is referred to the web version of this article.)

the zonal variations of temperature was derived from each year of observations. The results are summarized by their average value and standard deviation (Fig. 3A). The largest temperature variations are localized in longitude, with a peak value of nearly 6 K at 240°E . A superposition of zonal harmonics is required to represent this type of wave structure. The standard deviation is only 0.5 K, and some of this comes from measurement noise, so the year-to-year variations in wave properties are remarkably small.

The average waveform in Fig. 3A does not vary significantly when the upper boundary of the wavenumber range is increased from 24 to 30. Analysis of other subsets of data supports this conclusion. We therefore set the upper boundary to $m = 24$ for all results reported here. The lower boundary of the wavenumber range ($m = 8$) serves to isolate the waves of interest from other waves, such as the non-migrating tides discussed in Section 1, for which $m < 5$. The specific reason for choosing $m = 8$ is explained in Section 4.1.

The MCS limb observations are sensitive to waves that satisfy two conditions. First, the vertical wavelength must exceed 10 km, twice the vertical resolution of the retrieved temperature profiles. Second, the horizontal wavelength must exceed about 700 km, twice the line-of-sight resolution of observations at the limb, to ensure that the waves are detected in both the in-track and cross-track observations.

The method of analysis imposes a third condition on the spatial structure of the waves: the zonal wavenumber must be within the range used to reconstruct the waveform ($m = 8$ –24). Consider the effect of this condition on a wave with a horizontal wavelength of 1400 km (a 24° arc of a great circle), like the ones observed by MCS (Section 4.1). The zonal wavenumber depends on the orientation of the wavefronts; it ranges from $m = 15$ for a wave traveling due east to $m = 0$ for a wave traveling due north. For a minimum zonal wavenumber of $m = 8$, this condition prevents detection of waves whose direction of propagation is within about $\pm 30^\circ$ of north or south. The exact limit depends on the shape of the wavefronts (e.g., straight lines or concentric circles).

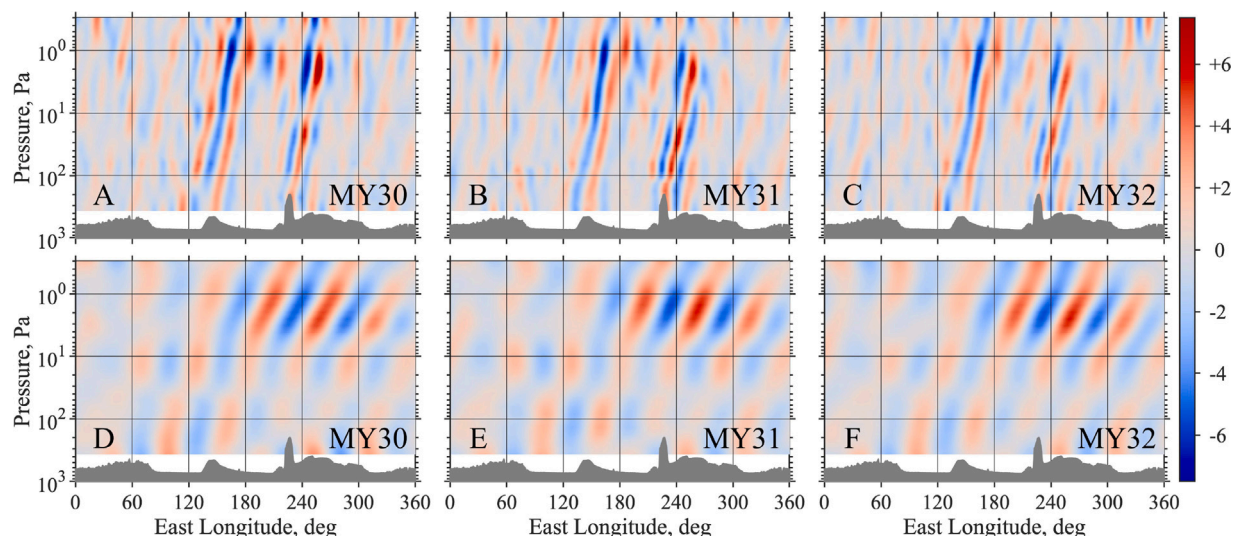


Fig. 4. Longitude-pressure cross sections of wave-induced temperature variations observed by MCS. Results are shown in wavenumber ranges of (A–C) $m = 8\text{--}24$ and (D–F) $m = 5\text{--}7$. Each row compares results from different years at the same season ($L_s = 90^\circ$), latitude (21°N), and local time (3 h). The units on the color bar are K. (For interpretation of the references to color in this figure legend, the reader is referred to the web version of this article.)

We performed a sensitivity study to see how a data gap would affect the results in Fig. 3A. Data were excluded from a 20° longitude band centered at 300°E (like the one in Fig. 2A) and the analysis was repeated. Fig. 3B shows how the new fit differs from the previous version in each of the 7 years. The fits are unreliable in and around the longitude band where data were removed, but they are essentially unchanged at other longitudes. By allowing wild excursions within the gap, a slightly better fit is obtained to data outside the gap. This illustrates the importance of the cross-track and off-track profiles, which markedly improve the quality of the results by filling gaps in the in-track profiles.

Least-squares analysis involves a matrix inversion. The condition number of the matrix has a value of 1 (well-conditioned) for each example shown in Fig. 3A. When a longitude gap is introduced (Fig. 3B), the condition number increases to 34, flagging the results as dubious. To avoid errors of this sort, we reject any result where the condition number exceeds 5.

The cross-track and in-track profiles sample different local times, but this has little effect on the results reported here. At low latitudes, the separation in local time between the cross-track and in-track profiles is ± 1.5 h (Kleinböhl et al., 2013). This corresponds to $\pm 45^\circ$ of phase for a semidiurnal wave and half as much for a diurnal wave. When comparable numbers of right and left cross-track profiles are available in each bin, their average will be close to the in-track temperature. That is generally the case; in observations from MY29–35, one side has more than twice as many samples as the other side in only 11% of the bins.

In addition to analyzing each year separately, we also analyzed the data collectively. The resulting wave climatology is based on nearly 7 years of observations (MY29–35); one season was excluded ($L_s = 180\text{--}270^\circ$ of MY34) to avoid the planet-enshrouding dust storm. As noted above, a separate set of bins was retained for each year of observations, and the data in each bin were conditioned by averaging the samples within 4° windows of longitude. This ensures that all bins from all years are weighted equally in the least-squares solution, regardless of how many samples they contain. Without this conditioning, the year-to-year variations in the density of data, which are considerable, would have distorted the climatology. Figures shown in Section 4 are from the climatology unless labeled with a year number.

A similar method was used to characterize the waves in the numerical simulation. First, the field of interest (e.g., temperature or zonal wind speed) was sampled at fixed local time so that the results can be

compared directly to those derived from the MCS data. As the output from the MGCM has been mapped to a uniform horizontal grid, the zonal structure of the waves can be obtained through Fourier analysis. The approach differs from the one applied to the MCS data in that analysis of the simulation was carried out on model levels rather than surfaces of constant pressure. The model levels never intersect the surface, allowing analysis to be extended all the way to the ground.

4. Results

4.1. General properties

We used the method of analysis described in Section 3 to extract new information about atmospheric waves from the MCS temperature measurements. For example, Fig. 4 shows the waves observed by MCS in two wavenumber ranges that have received little previous attention, $m = 8\text{--}24$ and $m = 5\text{--}7$. Results are shown from three successive years at the northern summer solstice ($L_s = 90^\circ$) in a 6° latitude band centered at 21°N , between Olympus Mons and Elysium Mons. The local time is 3 h; we focus on nighttime profiles because they extend to lower altitudes than daytime profiles at this season. Interannual variations are remarkably small in both ranges of m . The peak amplitude is about 8 K at $m = 8\text{--}24$ (Fig. 4A–C) and 6 K at $m = 5\text{--}7$ (Fig. 4D–F). The group velocity is nearly parallel to the wavefronts (see Section 3), eastward and upward in both ranges of m for a wave excited at the surface. We refer to this configuration of the wavefronts as an eastward tilt.

The waves in Fig. 4A–C are what we refer to as DWPs; the wave in Fig. 4D–F is possibly a nonmigrating tide. They are distinct from one another in that the slope of the wavefronts differs by about a factor of two at pressures less than 10 Pa, where the amplitude is large. In addition, the wave in Fig. 4D–F is less localized in longitude than the waves in Fig. 4A–C, which appear to emanate from Elysium Mons and Olympus Mons.

The signature of the waves also appears in MCS measurements of water-ice opacity, as shown in Fig. 5. This cross section of cloud structure was obtained by binning the opacity data and averaging the samples within each bin. The temperature contours show the deviation from the zonal mean ($m = 1\text{--}24$), including contributions from both DWPs and nonmigrating thermal tides. Wave-induced adiabatic heating creates a narrow, sloping gap in the water-ice cloud at 150°E , above Elysium Mons, as well as modulation of the cloud structure above Olympus Mons at pressures of 10–30 Pa. The width of the gap above

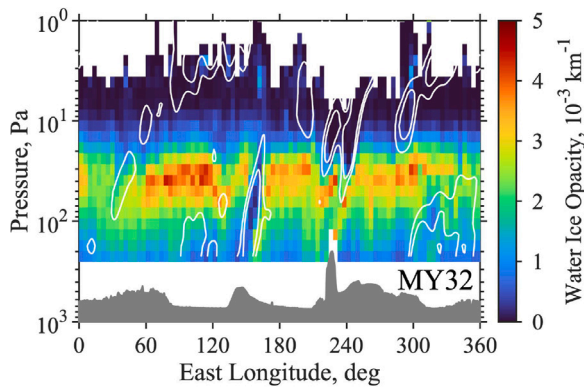


Fig. 5. Longitude-pressure cross sections of water-ice opacity (color shading) and wave-induced temperature variations (white contours) observed by MCS in MY32. To avoid clutter, contours of temperature are shown only at +2 and +4 K. The observations are from $L_s = 90^\circ$ of MY32 at the same latitude (21°N) and local time (3 h) as in Fig. 4. The results from other years look essentially the same. (For interpretation of the references to color in this figure legend, the reader is referred to the web version of this article.)

Elysium indicates that it arises primarily from a DWP. This modulation of cloud structure confirms that the waves are localized in longitude. Fig. 5 also illustrates the accuracy and internal consistency of the MCS retrievals.

Fig. 6 shows a complementary view of the wave structure. These MCS observations are from the southern summer solstice ($L_s = 270^\circ$) at the 2.5-Pa pressure level. The local time is 3 h. (The daytime observations are discussed below.) As in Fig. 4, the wave structure repeats closely from year to year. The peak amplitude is about 15 K at $m = 8\text{--}24$ (Fig. 6A–C) and 7 K at $m = 5\text{--}7$ (Fig. 6D–F). In both cases the waves are confined to low latitudes, but the horizontal structure is different in the two ranges of m . The wave in Fig. 6D–F is broader in latitude and less localized in longitude than the DWPs in Fig. 6A–C, which supports our decision to partition the waves. In the remainder of this paper, we focus on wave activity at $m = 8\text{--}24$.

The DWPs are localized, which allows the sources to be identified, as shown in Fig. 7. For example, waves emanate from Elysium Mons and the western rim of Isidis Planitia at $L_s = 18^\circ$ (Fig. 7A and 7D), from Elysium Mons and Olympus Mons at $L_s = 63^\circ$ (Fig. 7B and 7E), and from Pavonis Mons and Arsia Mons at $L_s = 315^\circ$ (Fig. 7C and 7F). Some wavefronts in Fig. 7F are aligned with the Tharsis Montes, tilting from southwest to northeast, which suggests that the three volcanoes act collectively to excite waves. This is confirmed by the MGCM simulation, as discussed in Section 4.2.

The spatial distribution of the DWPs varies strongly with L_s . For example, waves appear near the western rim of Isidis Planitia at $L_s = 18^\circ$ (Fig. 7A and 7D) but not at $L_s = 63^\circ$ (Fig. 7B and 7E). Similarly, waves are present near Elysium Mons and Olympus Mons at $L_s = 63^\circ$ (Fig. 7B and 7E) but not at $L_s = 315^\circ$ (Fig. 7F). In Fig. 7F, waves also appear near the southern rim of Isidis Planitia and in the southern tropics at longitudes of $60\text{--}210^\circ\text{E}$; this region was inactive at $L_s = 63^\circ$. In general, wave activity shifts from the northern tropics at $L_s = 63^\circ$ (Fig. 7E) to the southern tropics at $L_s = 270^\circ$ (Fig. 6A–C) and $L_s = 315^\circ$ (Fig. 7F). These variations in the spatial distribution of the DWPs are caused in part by seasonal changes in the boundary-layer forcing (Section 4.2).

Several other characteristics of the DWPs are apparent in Fig. 7. First, the vertical wavelength is about 40 km, easily resolved by MCS. Second, the zonal wavenumber m is about 15 (when observed at fixed local time), corresponding to a zonal wavelength of about 1400 km. This result was derived by computing the autocorrelation of the wave-induced temperature variations in cross sections of wave structure like

those in Fig. 7A–F. Third, the tilt of the wavefronts varies with season, from westward at $L_s = 18^\circ$ to eastward at $L_s = 63^\circ$ and 315° . As we show in Section 4.3, the direction changes in response to the seasonal evolution of the diurnal-mean zonal winds in the tropics. Note that the true angle between the wavefronts and the horizon is much smaller than it appears in Fig. 7, where the vertical axis has been stretched. Finally, Fig. 7 compares longitude-latitude cross sections at the same pressure and season but different local times, which shows that the wave amplitude varies with time of day. In each case, the amplitude is 2–3 times larger at 3 h (Fig. 7D–F) than at 15 h (Fig. 7G–I).

The preceding results can be used to evaluate the performance of the MGCM. It is instructive to begin with a closer look at the method of analysis used to characterize the simulated DWPs. The results in Fig. 8A–C were obtained from Fourier analysis on MGCM model levels, as described at the end of Section 3. As a test of this procedure, we used the method of analysis applied to the MCS data to derive a second version of the longitude-pressure cross sections. Specifically, output from the simulation (at fixed local time) was interpolated to surfaces of constant pressure, using the same pressure levels as the MCS data, and least-squares analysis was used to determine the zonal structure of the waves at each pressure level; the results appear in Fig. 8D–F. There are no significant differences between the two versions of the cross sections. This confirms that the MCS results in Fig. 7A–C can be compared directly with the MGCM results in Fig. 8A–C, despite differences in how they were derived.

There is a strong resemblance between the DWPs observed by MCS (Fig. 7A–C) and the ones that appear in the simulation (Fig. 8A–C) at similar (but not identical) combinations of L_s , latitude, and local time. The amplitudes are comparable; the waves are localized; the implied sources are the same as the ones identified in Fig. 7; and the tilt of the wavefronts varies with season. In Fig. 8A–C, the values of L_s , latitude, and local time have been tuned to yield closer agreement with Fig. 7A–C, respectively. Relatively small adjustments are sufficient to align the simulation with the measurements, which confirms that the MGCM is performing reasonably well. The DWPs are difficult to simulate because of their sensitivity to the diurnal-mean zonal winds and the diurnal cycle of boundary-layer slope flows, as discussed later in this section.

We examined the diurnal cycle of the simulated waves by constructing Hovmöller diagrams. Fig. 8G–I show how the waves evolve with longitude and local time at the pressure levels marked in Fig. 8A–C, respectively. This illustrates four points. First, the waves travel westward (Fig. 8G) or eastward (Fig. 8H and 8I) relative to the surface. In that respect, they differ from orographic lee waves, which are stationary. The zonal phase speed is about -25 m s^{-1} in Fig. 8G and $+25\text{ m s}^{-1}$ in Fig. 8H and 8I. Second, the wavefronts tilt in the direction of propagation. Third, the wave amplitude at constant pressure varies strongly with time of day, as it did in Fig. 7. This indicates the presence of wave packets — a diurnal pulse — rather than steady oscillations. Finally, the wave oscillations are roughly semidiurnal, as shown by the Hovmöller diagrams and implied by the combination of zonal wavelength ($\sim 1400\text{ km}$) and zonal phase speed ($\sim 25\text{ m s}^{-1}$).

As discussed in Section 3, the MCS temperature measurements were separated into bins by L_s , latitude, pressure, and local time. Spectral analysis of the data within each bin yields a composite waveform of temperature versus longitude like the one in Fig. 3A. To quantify the level of wave activity, we took the absolute value of the waveform in each bin and found its maximum value (5.5 K for the example in Fig. 3A). We refer to this as the peak amplitude.

Waves originating from a specific surface feature can be characterized by computing the peak amplitude within a restricted longitude range. For example, Fig. 9 shows results from within a 100° longitude band centered on Elysium Mons. The season is $L_s = 90^\circ$, when Elysium is an active source of waves (Fig. 4A–C). In MCS measurements at 3 h local time (Fig. 9A), the peak amplitude at the 1-Pa pressure level (8 K) is significantly larger than its value near the surface (2 K), as expected for a wave that conserves energy as it propagates vertically

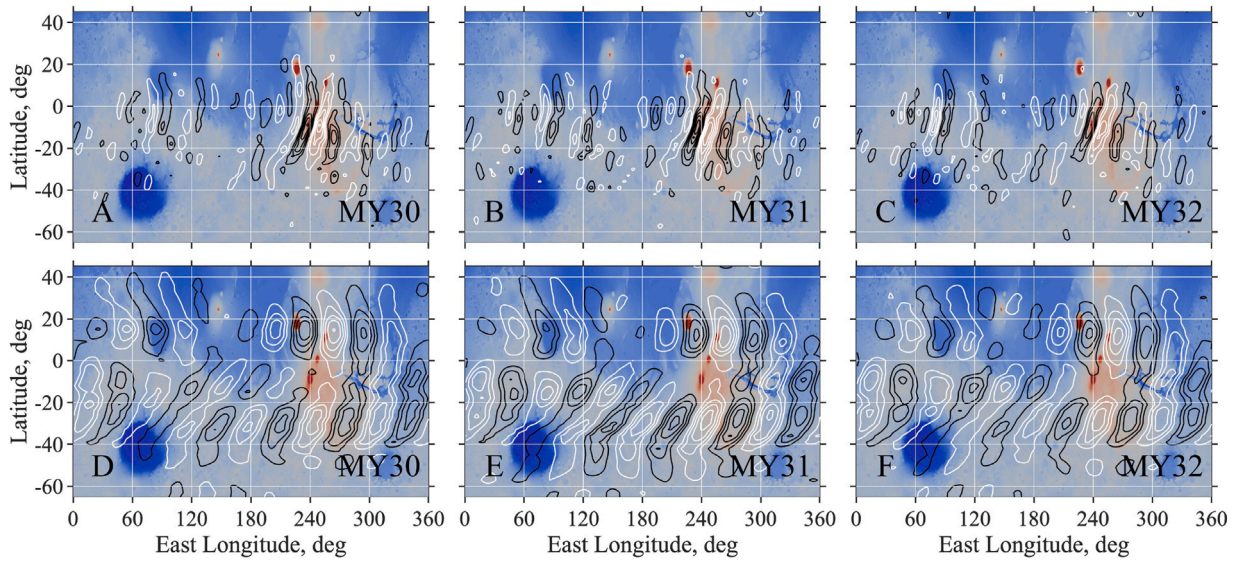


Fig. 6. Longitude-latitude cross sections of wave-induced temperature variations observed by MCS. Results are shown in wavenumber ranges of (A–C) $m = 8$ –24 and (D–F) $m = 5$ –7. Each row compares results from different years at the same season ($L_s = 270^\circ$), pressure level (2.5 Pa), and local time (3 h). Temperature contours are shown at intervals of (A–C) 3 K and (D–F) 1.5 K, with positive contours in white and negative contours in black. Surface topography is shown by color shading. (For interpretation of the references to color in this figure legend, the reader is referred to the web version of this article.)

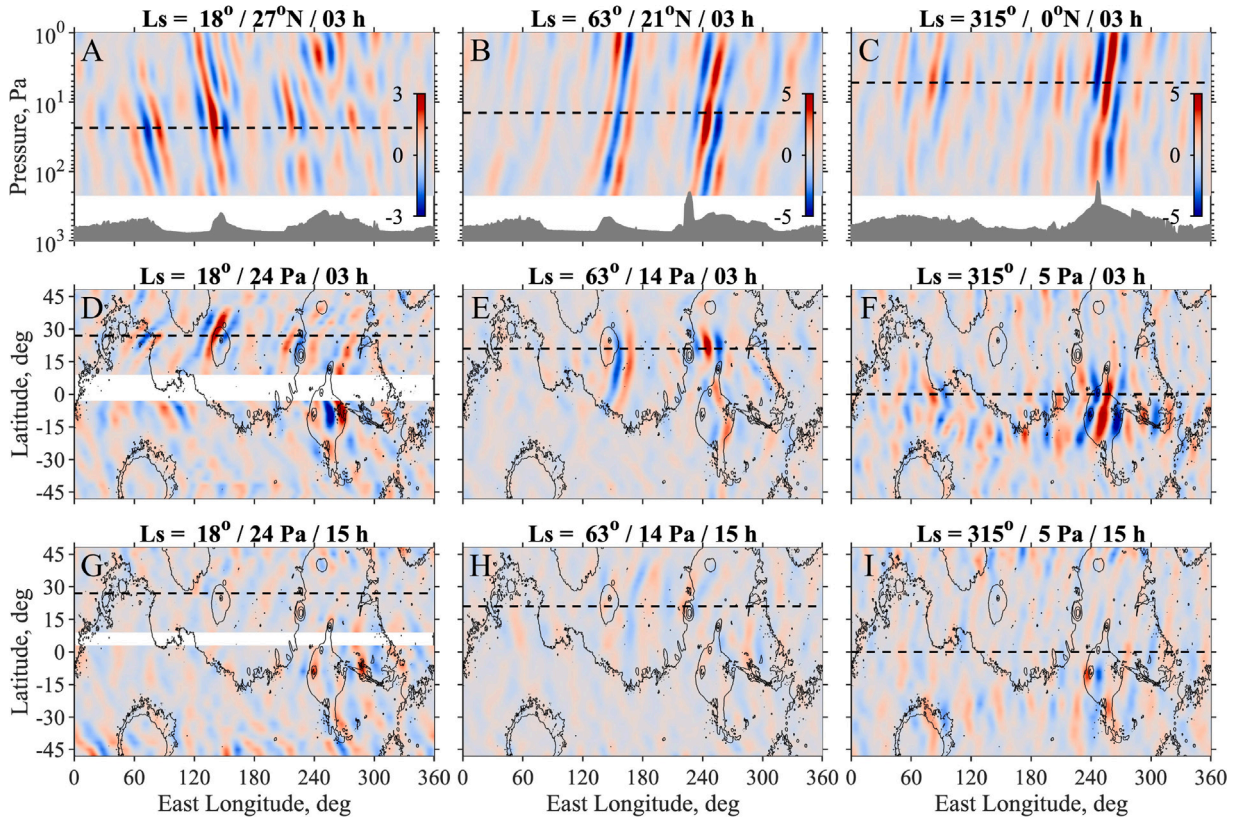


Fig. 7. Wave-induced temperature variations ($m = 8$ –24) observed by MCS at (A, D, G) $L_s = 18^\circ$; (B, E, H) $L_s = 63^\circ$; and (C, F, I) $L_s = 315^\circ$. The local time is (A–F) 3 h and (G–I) 15 h. Three cross sections are shown at each value of L_s , one at constant latitude (A–C) and the two at constant pressure (D–I). The temperature variations are shown by color shading. The color bars in A–C apply to the other cross sections at the same L_s ; the units are K. The horizontal black lines in A–C indicate the pressure level in D–I. The horizontal black lines in D–I indicate the latitude in A–C. These results are from the 7-year MCS climatology. (For interpretation of the references to color in this figure legend, the reader is referred to the web version of this article.)

through a density-stratified medium. The reason for the rapid decrease in peak amplitude above the 1-Pa pressure level is not known. It could be a consequence of wind shear or vertical variations in static stability, which modulate the vertical component of the group velocity.

Interpretation of observations at fixed local time, such as those in Fig. 9A, is also complicated by the presence of wave packets.

We characterized the waves in the MGCM simulation in the same way, obtaining results analogous to those in Fig. 9A at 1-h intervals of

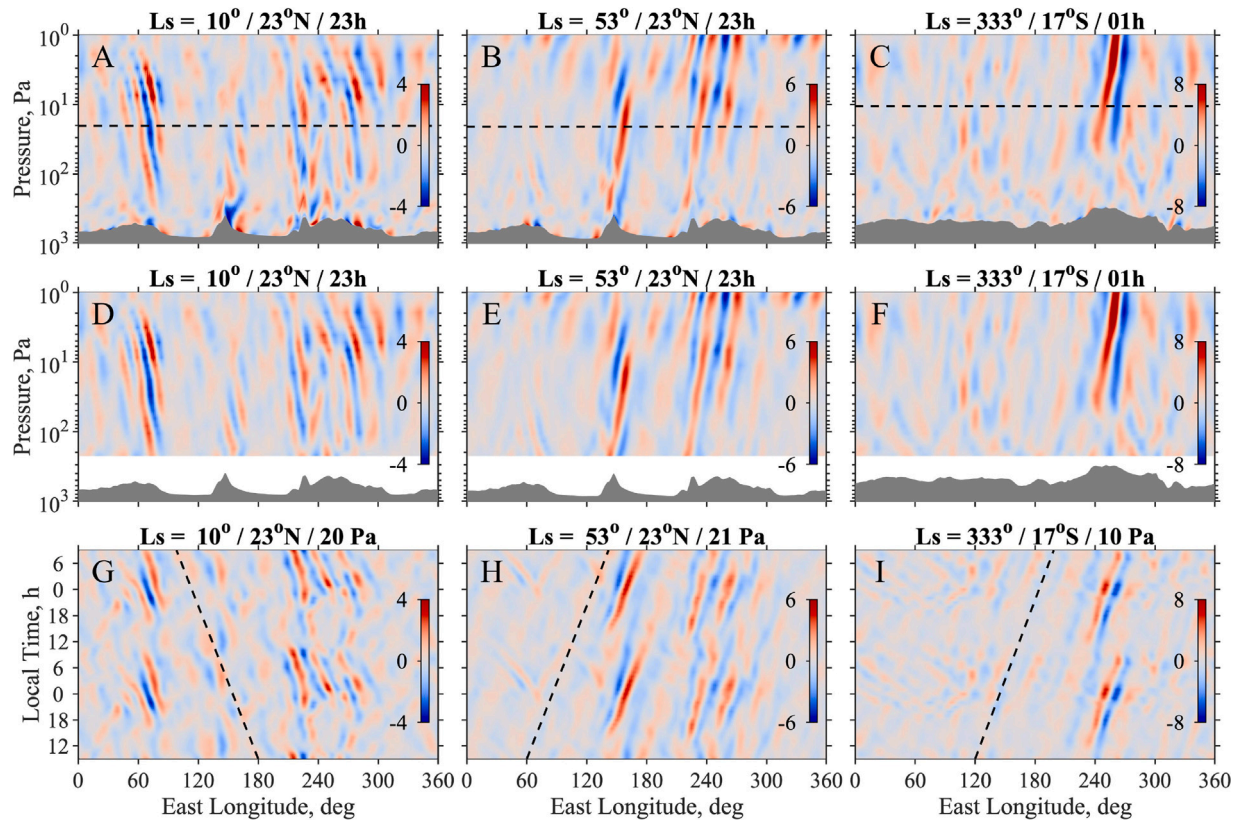


Fig. 8. MGCM simulation of DWPs at three combinations of season and latitude: (A, D, G) $L_s = 10^\circ$, 23°N ; (B, E, H) $L_s = 53^\circ$, 23°N ; and (C, F, I) $L_s = 333^\circ$, 17°S . The temperature variations are shown by color shading. The units on the color bars are K. The results in A–C were derived through Fourier analysis on MGCM model levels; those in D–F were derived through least-squares analysis on surfaces of constant pressure. Each longitude–pressure cross section in the top row includes a horizontal dashed line that indicates the pressure level of the corresponding Hovmöller diagram in the bottom row. The dashed lines in G–I indicate zonal phase speeds of (G) -25 m s^{-1} and (H, I) $+25\text{ m s}^{-1}$. These results were derived from 5-sol averages of output from the MGCM simulation. Each Hovmöller diagram shows two cycles through the same average sol. (For interpretation of the references to color in this figure legend, the reader is referred to the web version of this article.)

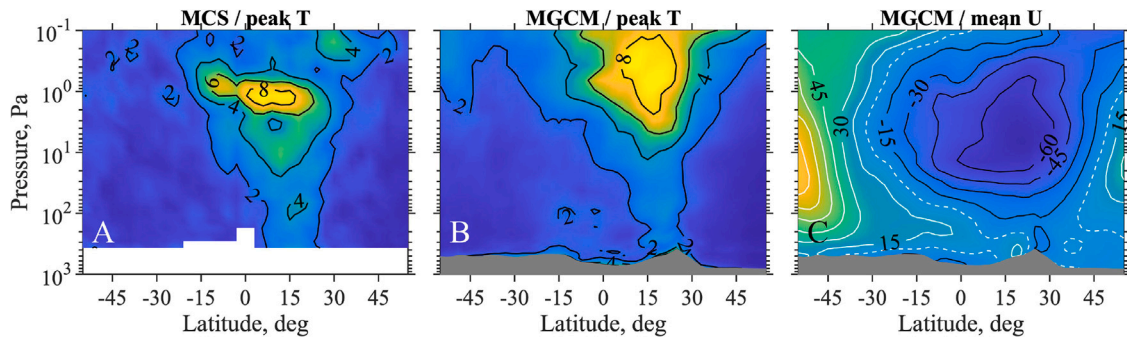


Fig. 9. (A) The peak amplitude of waves observed by MCS at $L_s = 90^\circ$; the local time is 3 h. (B) The corresponding diurnal-mean peak amplitude from the MGCM simulation at $L_s = 89^\circ$. Both results are from a 100° longitude band centered on Elysium Mons. The contour interval is 2 K. (C) The diurnal-mean zonal winds at 145°E in the MGCM simulation at $L_s = 89^\circ$. The contour interval is 15 m/s. The dashed white line is the zero contour.

local time. The diurnal-mean peak amplitude of the simulated waves is shown in Fig. 9B; variations with time of day are discussed in Section 4.2. The simulation is generally consistent with the MCS measurements. At low altitudes, the peak amplitude exceeds 2 K only in the northern tropics ($15\text{--}30^\circ\text{N}$), implying that Elysium Mons is the primary source of the waves.

Fig. 9C places the waves into context with the diurnal-mean zonal winds. At low latitudes, the winds are predominantly westward, with a magnitude that exceeds 60 m s^{-1} at pressures of 1–20 Pa. The peak amplitudes in Fig. 9A and 9B are largest at about 15°N , so that the wave propagates vertically through the center of the westward equatorial jet. A Hovmöller diagram (not shown) indicates that the wave is traveling eastward with respect to the surface, like the one in Fig. 8H. Although

waves traveling upstream can decelerate the mean winds in the region where they dissipate (Fritts and Alexander, 2003), the impact of the DWPs on the general circulation is constrained by their confinement in longitude.

4.2. Diurnal cycle and forcing mechanism

In this section we use the MGCM simulation to characterize the diurnal cycle of wave activity and to identify the forcing mechanism. We focus initially on Elysium Mons, which is bordered on all sides by extensive plains. This isolation makes the dynamics easier to interpret.

Considerable insight can be gained from longitude–height cross sections of the zonal and vertical components of the simulated wind

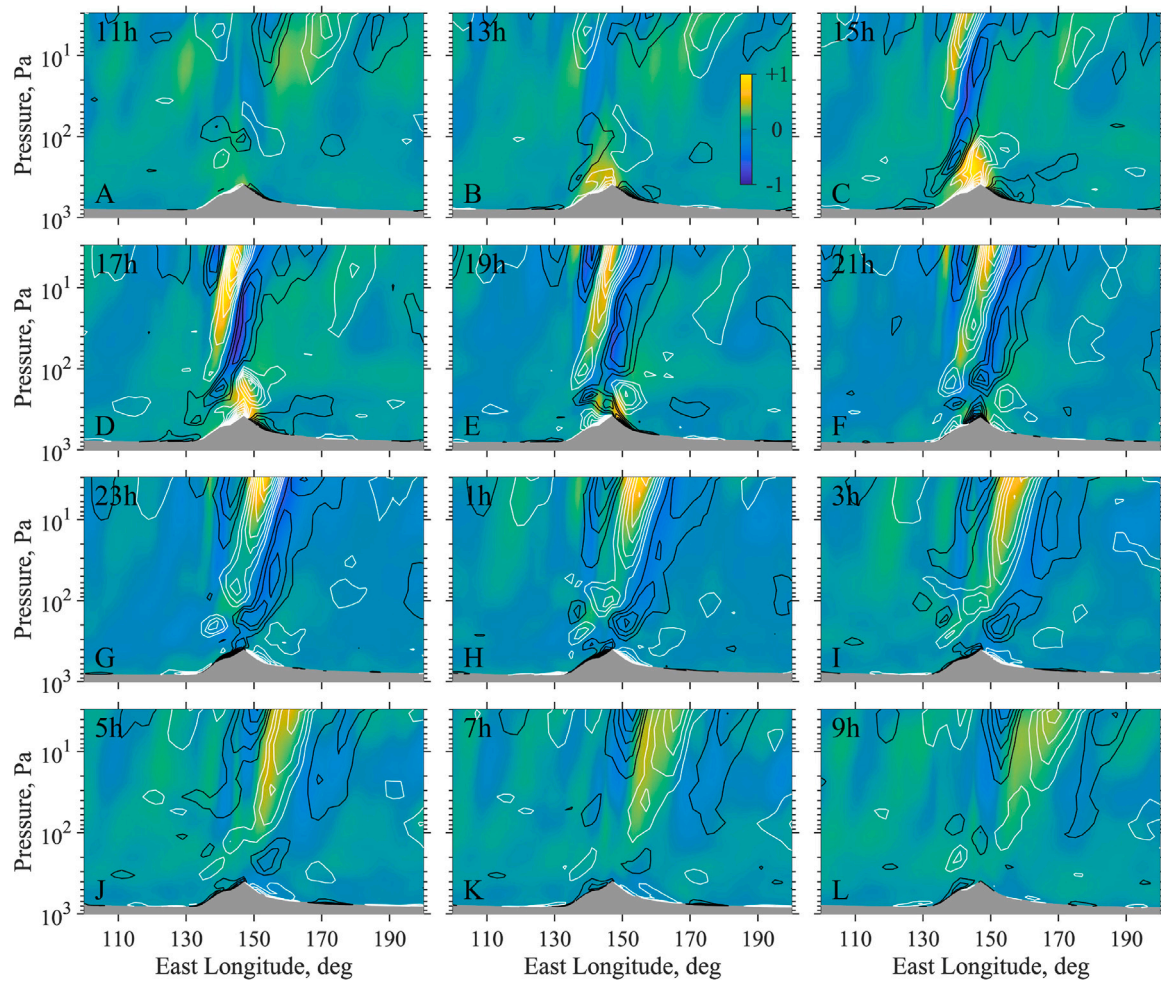


Fig. 10. Longitude-height cross sections of the zonal and vertical winds in the MGCM simulation at $L_s = 89^\circ$. The latitude is 23°N , slightly south of Elysium Mons. Each panel samples the diurnal cycle at fixed local time; the interval between panels is 2 h. The zonal component of the wind field is shown by contours. The contour interval is 3 m s^{-1} , with positive contours in white and negative contours in black. The vertical component of the wind field is shown by color shading. The color bar in B applies to all panels; the units are m s^{-1} . (For interpretation of the references to color in this figure legend, the reader is referred to the web version of this article.)

field. The results in Fig. 10 are from $L_s = 89^\circ$ at 23°N , the parallel that bisects the pedestal on which Elysium stands. The full vertical wind field is shown, with no restrictions on the wavenumber range; the diurnal average and the contributions from thermal tides ($m < 8$) have been removed from the zonal winds. Both components of the wind field vary noticeably the in 2-h interval of local time between successive panels. The wave in the simulation resembles the one observed near Elysium Mons at the same season (Fig. 4A–C). In both cases, the wave is localized in longitude, and the wavefronts tilt eastward with height. The zonal and vertical wavelengths of the simulated wave are also consistent with the MCS observations.

The diurnal cycle of wave activity proceeds as follows. At 11 h (Fig. 10A), upslope winds are present in a very shallow layer adjacent to the surface on both sides of the pedestal. Wave activity is limited to pressures less than 10 Pa. At 13 h (Fig. 10B), the upslope flow is deeper and stronger; its magnitude exceeds 12 m s^{-1} on both sides of the pedestal. Rising motion develops in the lowest 5 km above the surface at $140\text{--}150^\circ\text{E}$, where the upslope flows converge. The zonal winds reverse direction at higher altitudes above both slopes as air returns to the surrounding plains in a deep layer at pressures of 50–300 Pa. At 15 h (Fig. 10C), the rising motion at $140\text{--}150^\circ\text{E}$ is deeper, and its speed has increased to 1 m s^{-1} . An eastward-tilting wave emerges from the westward-facing slope ($135\text{--}145^\circ\text{E}$). The timing implies that the wave is forced by the upward surge in the vertical winds, which generates

negative buoyancy as it penetrates into layers of stable stratification. At 17–21 h (Fig. 10D–F), the wave extends throughout the vertical range of the figure. Upward winds in the lowest scale height above the pedestal become steadily weaker and are largely absent at 21 h. At 1–5 h (Fig. 10H–J), the winds in the lowest few kilometers above the surface have reversed direction, and air is flowing downhill. The winds in the lowest scale height are too weak to excite waves, and waves excited earlier in the day have propagated to higher altitudes. By 11 h (Fig. 10A), the wave is largely absent from the lower atmosphere. (An animation of the diurnal cycle in Fig. 10 can be found at the end of this article in Supplementary Data.)

Both Elysium Mons and the pedestal on which it stands contribute to the wave forcing, as shown in Fig. 11. Two model levels are considered; one is $0.07 H$ above ground level (AGL) and the other is $0.53 H$ AGL, where H is the pressure scale height ($\sim 10 \text{ km}$). In the late afternoon, the horizontal winds near the surface ($0.07 H$ AGL) are predominantly in the upslope direction (Fig. 11A). Their speed exceeds 15 m s^{-1} across most of pedestal, with a maximum of more than 45 m s^{-1} . The zonal and meridional components of the wind field make similar contributions to the overall pattern. The horizontal convergence of the near-surface winds generates strong upward winds above the pedestal (Fig. 11B). The vertical wind speed at $0.53 H$ AGL exceeds $+0.5 \text{ m s}^{-1}$ in a region that extends from 18°N to 29°N and 141°E to 150°E , directly above the near-surface convergence zone.

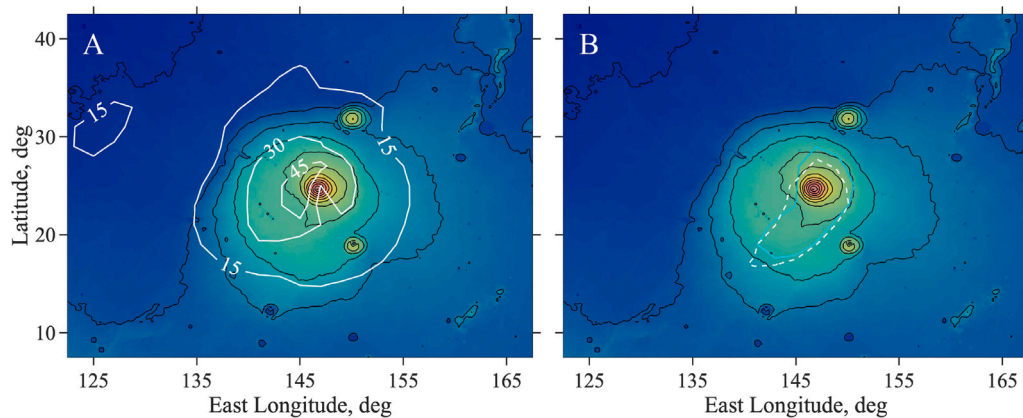


Fig. 11. Aspects of the wind field near Elysium Mons in the MGCM simulation at $L_s = 89^\circ$. The local time is 17 h. Surface topography is shown by color shading and black contours; the contour interval is 1.5 km. (A) The horizontal wind speed at 0.07 H AGL is shown by white contours; the units are m s^{-1} . (B) The dashed white line marks the boundary of a region of strong convergence of the horizontal winds at 0.07 H AGL ($> 6 \text{ m s}^{-1}$ per degree). This convergence zone produces strong upward winds at 0.53 H AGL, which exceed $+0.5 \text{ m s}^{-1}$ within the cyan contour. The wind field in both panels is taken directly from the simulation, without filtering or removal of diurnal or zonal averages. (For interpretation of the references to color in this figure legend, the reader is referred to the web version of this article.)

In summary, Figs. 10 and 11 show that the DWPs arise from horizontal convergence of the near-surface winds. This type of forcing is restricted to local times of about 13–18 h, which explains the presence of wave packets rather than steady oscillations. These results are not particularly sensitive to the horizontal resolution of the simulation — the 900-km-diameter pedestal is well resolved in the baseline C48 simulation, where the grid spacing is $\sim 110 \text{ km}$ ($\sim 1.9^\circ$ of latitude). Both the convergence zone and the wave it excites look essentially the same in a C192 simulation with a grid spacing of $\sim 30 \text{ km}$.

We identified other sources of this type of wave by mapping the horizontal convergence of the near-surface winds in the MGCM simulation. Fig. 12 shows the results at the solstices. In both cases, convergence is generally stronger in the summer hemisphere than in the winter hemisphere, particularly at longitudes of 0 – 210°E . Regions of convergence are highly localized, as reflected by the tightly nested contours.

Long, narrow convergence zones form in connection with steeply sloped topography. At the northern summer solstice (Fig. 12A), the most notable examples are a crescent-shaped convergence zone along the rim of Isidis Planitia; a linear zone aligned with the Tharsis Montes; and a particularly long zone that traces the southern boundary of Valles Marineris at one end and the western boundary of Lunae Planum at the other. At the southern summer solstice (Fig. 12B), the convergence zone adjacent to Isidis Planitia has largely vanished, whereas the southern tropics have become more active. For example, there are numerous convergence zones south of the equator in a 180° longitude band centered on Tyrrhena Terra, a region that was relatively quiet in Fig. 12A. In addition, a long, crescent-shaped convergence zone has developed along the arc of elevated terrain that borders Solis Planum; this feature was weaker and discontinuous at the northern summer solstice.

Some of the convergence zones in Fig. 12 arise from an afternoon surge of air out of canyons and basins. This phenomenon has been studied previously through high-resolution simulations with the Oregon State University Mars Mesoscale Model (OSU MMM), one at $L_s = 151^\circ$ (Tyler and Barnes, 2015) and another at $L_s = 40^\circ$ (Hinson et al., 2019). The results in Fig. 12 are generally consistent with those simulations, which showed that convergence zones form in the afternoon along the southern boundary of central Valles Marineris (Tyler and Barnes, 2015) and along the rim of Isidis Planitia (Hinson et al., 2019). In both regions, convergence of the near-surface winds produces a strong surge in the vertical winds, but neither study assessed its importance as a source of atmospheric waves.

There is an important caveat to the results in Fig. 12. The simulation does not resolve convergence zones associated with small-scale surface

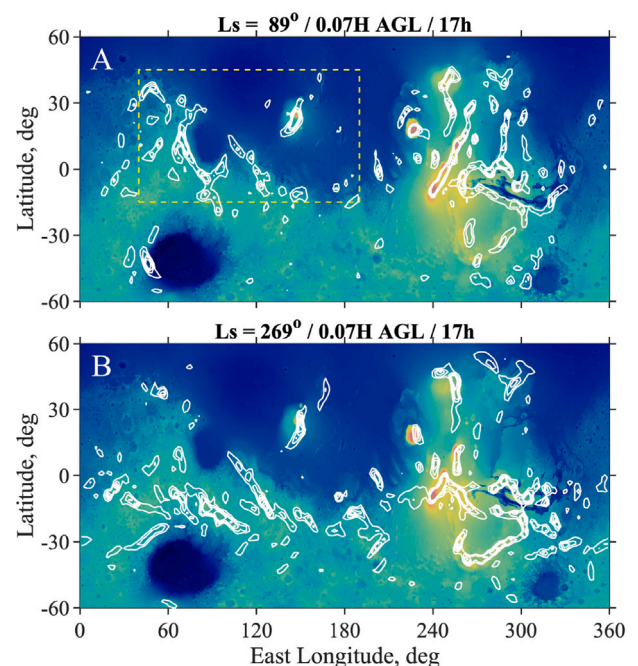


Fig. 12. Regions of strong convergence of the horizontal winds at 0.07 H AGL (white contours), as derived from the MGCM simulation at (A) $L_s = 89^\circ$ and (B) $L_s = 269^\circ$. The local time is 17 h. Contours are shown at intervals of 2.5 m s^{-1} per degree where the convergence is positive. Surface topography is shown by color shading. The region within the dashed lines in A is discussed below. (For interpretation of the references to color in this figure legend, the reader is referred to the web version of this article.)

features, such as the rim of Gale Crater and Mount Sharp (Tyler and Barnes, 2013), which are widely distributed on Mars. In many regions, the wave forcing is undoubtedly far more complex than the C48 simulation predicts. This complication is largely avoided at Elysium Mons, which is surrounded by relatively flat, featureless plains.

4.3. Propagation through the diurnal-mean zonal winds

The DWPs are strongly influenced by the spatial structure and seasonal evolution of the zonal wind field through which they propagate. In examining the nature of this dependence, we relied on the MGCM

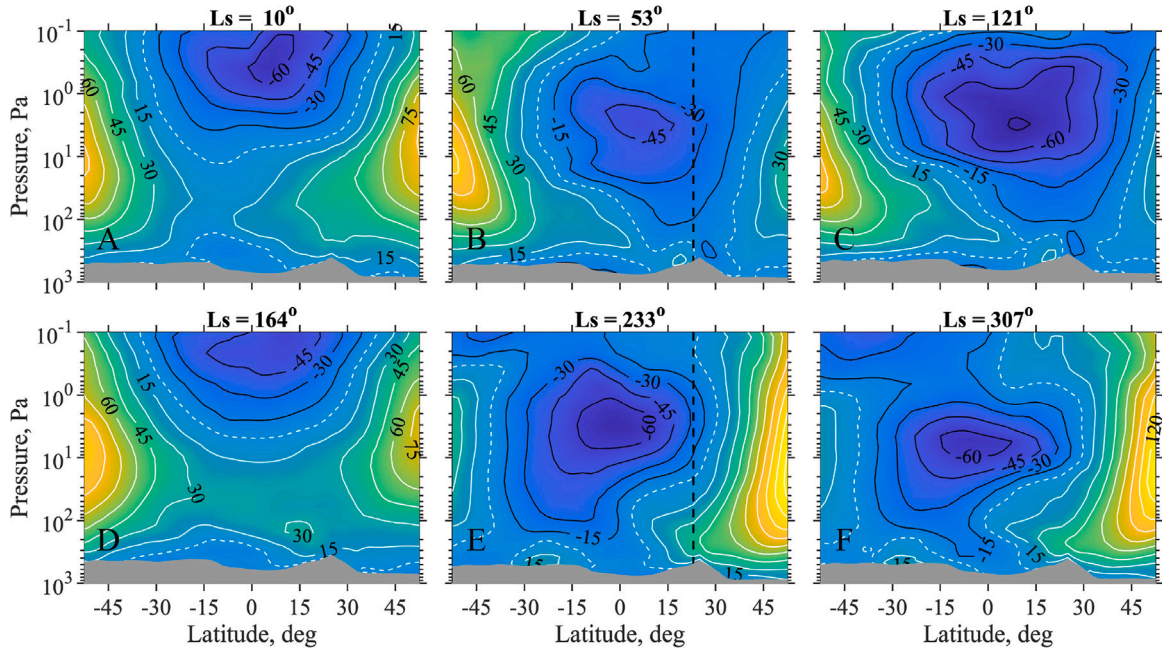


Fig. 13. The seasonal evolution of the diurnal-mean zonal wind field U at 145°E , as simulated by the MGCM. The contour interval is 15 m s^{-1} . The dashed white line is the zero contour. The dashed black lines in B and E mark latitudes used in subsequent figures.

to simulate the zonal winds, which have not been measured directly. Fig. 13 shows the diurnal-mean zonal wind field U on a meridian near Elysium Mons for six values of L_s . We are interested primarily in the seasonal evolution of the zonal winds in the northern tropics, which can be summarized as follows. Near the northern summer solstice (Fig. 13B and 13C), the winds above Elysium Mons are westward throughout this pressure range. This configuration persists from about $L_s = 40^\circ$ to 140° . Near the northern winter solstice (Fig. 13E and 13F), the winds above Elysium are eastward below the 20-Pa pressure level and westward at higher altitudes. This configuration persists from about $L_s = 220^\circ$ to 320° . Transitions between these two configurations occur near the equinoxes (Fig. 13A and 13D), when a low-altitude layer of eastward winds extends across the tropics, with overlying westward winds at pressures less than 5 Pa. This super-rotation at low altitudes results from forcing by the migrating diurnal tide (Lewis and Read, 2003).

Fig. 14 illustrates the behavior of the simulated DWPs at two of the seasons shown in Fig. 13. In the first case ($L_s = 233^\circ$), the diurnal-mean zonal winds in the northern tropics are eastward at low altitudes and westward at high altitudes, reversing direction near the 20-Pa pressure level (Fig. 14A). A prominent, westward-tilting wave appears above Elysium Mons. The properties of the wave suggest that its confinement to low altitudes, where U is eastward, is caused by a critical level (defined below). In the rest frame of the surface, the wave has a zonal phase speed u_p of -12 m s^{-1} , a period of ~ 1 sol, and a zonal wavelength λ_x of $\sim 1100 \text{ km}$ (Fig. 14B). In the rest frame of the fluid, the zonal phase speed is

$$\omega_i/k_x = u_p - U, \quad (5)$$

where ω_i is the fluid-relative “intrinsic” frequency, and $k_x = 2\pi/\lambda_x$. (In our sign convention, k_x is always positive and ω_i has the same sign as $u_p - U$.) The wave in Fig. 14A is presumably an inertia-gravity wave, which can propagate vertically only if $\omega_i^2 > f^2$ (Fritts and Alexander, 2003), where f is the Coriolis frequency. For a westward-traveling wave, the constraint is $\omega_i < -f$, which can be expressed as

$$u_p - U < -f/k_x = -9 \text{ m s}^{-1}, \quad (6)$$

where $f = 0.8 \Omega$ at 23°N . This condition is satisfied only where $U > -3 \text{ m s}^{-1}$, corresponding to pressures greater than 20 Pa in Fig. 14A. The

wave dissipates as it approaches the upper boundary of this range, where $\omega_i \rightarrow -f$, which is called a critical level (Fritts and Alexander, 2003), and there is no sign of the wave at higher altitudes (Fig. 14C). (The level spacing of the MGCM simulation is about 10 Pa near the critical level, so the dissipation of the wave is not resolved.)

Both the wave and the diurnal-mean zonal winds at Elysium Mons are much different at $L_s = 53^\circ$ (Fig. 14D–F). At this season, the winds at 23°N are westward throughout this pressure range, and a prominent eastward-tilting wave appears above Elysium Mons (Fig. 14D). In the rest frame of the surface, u_p is $+25 \text{ m s}^{-1}$, the wave period is about ~ 0.5 sols, and λ_x is $\sim 1100 \text{ km}$ (Fig. 14F). Vertical propagation is possible when

$$u_p - U > +f/k_x = +10 \text{ m s}^{-1}. \quad (7)$$

This condition is satisfied throughout the pressure range in Fig. 14D. In other words, westward winds do not prevent the vertical propagation of an eastward-traveling wave.

Another aspect of Fig. 14 is consistent with this interpretation. Elysium Mons also excites a westward-traveling wave at $L_s = 53^\circ$. It is a mirror image of the eastward-traveling wave in the Hovmöller diagram in Fig. 14E — the amplitude, period, and zonal wavelength are about the same but u_p has the opposite sign. In both cases, wave activity subsides at local times of 9–15 h, indicating the presence of wave packets like those in Fig. 8G–I. This westward-traveling wave encounters a critical level at about 70 Pa, where $U = -15 \text{ m s}^{-1}$, which accounts for its absence at higher altitudes (Fig. 14F).

Our interpretation of the results in Fig. 14 is based on a model for inertia-gravity waves that ignores the variation of f with latitude. However, models that account for this effect, such as the linear theory for equatorial waves (Andrews et al., 1987), lead to essentially the same conclusions.

In summary, Elysium Mons can excite waves traveling eastward or westward relative to the surface, as shown in Fig. 14. Their behavior is strongly influenced by wind shear because the zonal phase speed of the waves is relatively small compared with the wind speeds in Fig. 13. Waves are free to propagate vertically if u_p and U have opposite signs, whereas waves propagating in the same direction as U will generally be trapped below a critical level.

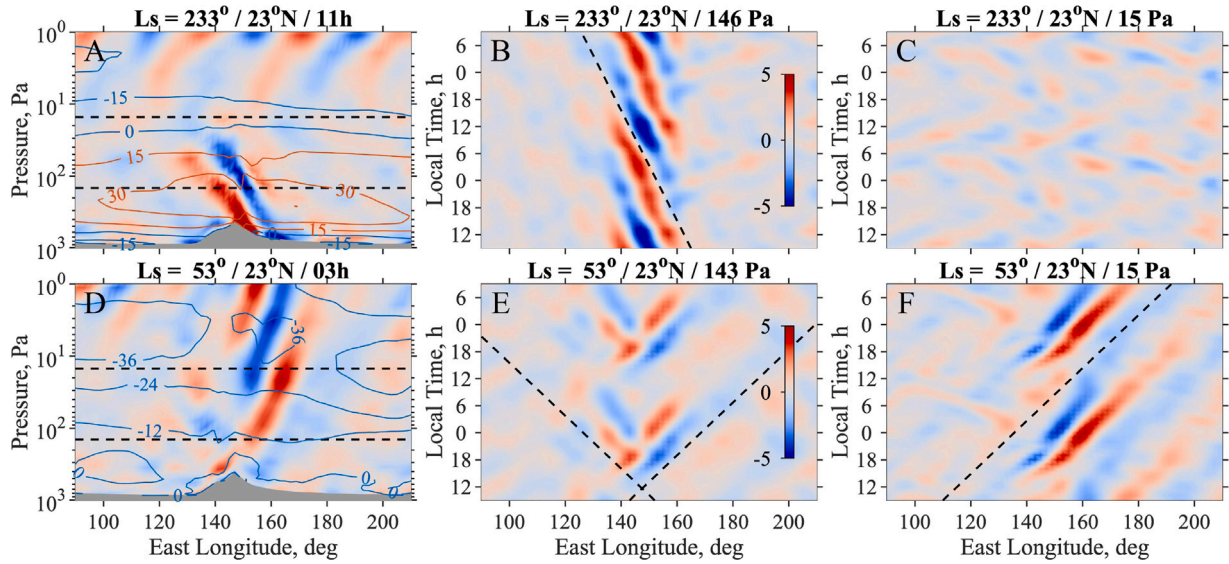


Fig. 14. (A–C) Characteristics of DWPs near Elysium Mons as simulated by the MGCM at $L_s = 233^\circ$. Wave-induced temperature variations are shown by color shading. The color bar in B also applies to A and C; the units are K. The diurnal-mean zonal winds (m s^{-1}) are shown by contours in A; orange and blue contours denote eastward and westward winds, respectively. Hovmöller diagrams in B and C show the diurnal cycle of the temperature variations at the pressure levels marked by dashed lines in A. (D–F) The corresponding results at $L_s = 53^\circ$. The dashed lines in the Hovmöller diagrams indicate zonal phase speeds of (B) -12 m s^{-1} , (E) $\pm 25 \text{ m s}^{-1}$, and (F) $+25 \text{ m s}^{-1}$. (For interpretation of the references to color in this figure legend, the reader is referred to the web version of this article.)

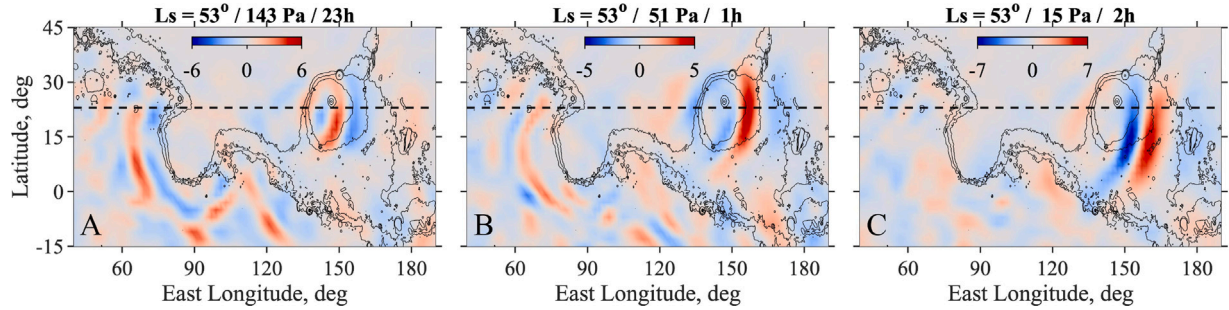


Fig. 15. Wave-induced temperature variations (color shading) in the MGCM simulation at $L_s = 53^\circ$. The units on the color bars are K. Results are shown at three model levels where the average pressure is (A) 143 Pa, (B) 51 Pa, and (C) 15 Pa. The local time is indicated above each panel. Black lines show a few contours of surface elevation, which were chosen to provide context without obscuring the waves. Dashed lines show the latitude of the results in Fig. 14. The region shown here is outlined by a dashed line in Fig. 12A. (For interpretation of the references to color in this figure legend, the reader is referred to the web version of this article.)

Fig. 15 shows longitude-latitude cross sections of the simulated waves at $L_s = 53^\circ$, providing further insight into the source of the waves and their filtering by the diurnal-mean zonal winds. The results in Fig. 15A are at the same model level as in Fig. 14E, where the average pressure is 143 Pa. There are two centers of wave activity. Both are closely aligned with convergence zones of the near-surface winds. (A map of the convergence zones at $L_s = 53^\circ$ closely resembles the one in Fig. 12A.) First, curving wavefronts are spreading outward from Elysium Mons, forming a bull's-eye pattern centered slightly southwest of the volcano. Fig. 14E illustrates the east–west symmetry of the wave structure at this pressure level. Second, crescent-shaped wavefronts are spreading outward from the convergence zone that traces the rim of Isidis Planitia.

Fig. 15 also shows how the waves evolve as they propagate vertically. The wave traveling eastward from Elysium Mons grows stronger with increasing height, and the wavefronts become broader. At the 15-Pa pressure level (Fig. 15C), the wave extends from about 30°N to the equator, in agreement with MCS observations at about the same season, pressure, and local time (Fig. 7E). Conversely, the westward-traveling waves at both Elysium and elsewhere are weaker in Fig. 15B than they were at lower altitudes (Fig. 15A), and they are absent from Fig. 15C, owing to filtering by a critical level. (An animation of Fig. 15

showing the full diurnal cycle can be found at the end of this article in Supplementary Data.)

We surveyed the MCS measurements to determine how the tilt of the wavefronts varies with latitude and season. The following procedure was applied to the data from each L_s -latitude bin. First, we constructed longitude-height cross sections of the wave-induced temperature variations like the ones in Fig. 7A–C, one for the dayside and one for the nightside. Contours were drawn at selected values of the temperature field, and the slope was calculated at locations distributed around the circumference of each contour. Finally, a histogram was assembled from the slopes on all contours on both the dayside and the nightside. We found that the median of this distribution gives a reliable indication of whether the wavefronts generally tilt eastward or westward; this was confirmed through visual inspection of longitude-height cross sections, as discussed below.

We applied this algorithm to the entire MCS dataset. The results appear in Fig. 16. Analysis was limited to pressures of 1–100 Pa, where profiles are widely available on both the dayside and the nightside. The temperature contours were set to $\pm 33\%$ of the peak amplitude within the relevant L_s -latitude bin. This is a compromise between contours at lower levels, which are more susceptible to noise, and contours at higher levels, which are not as long. We repeated the analysis using

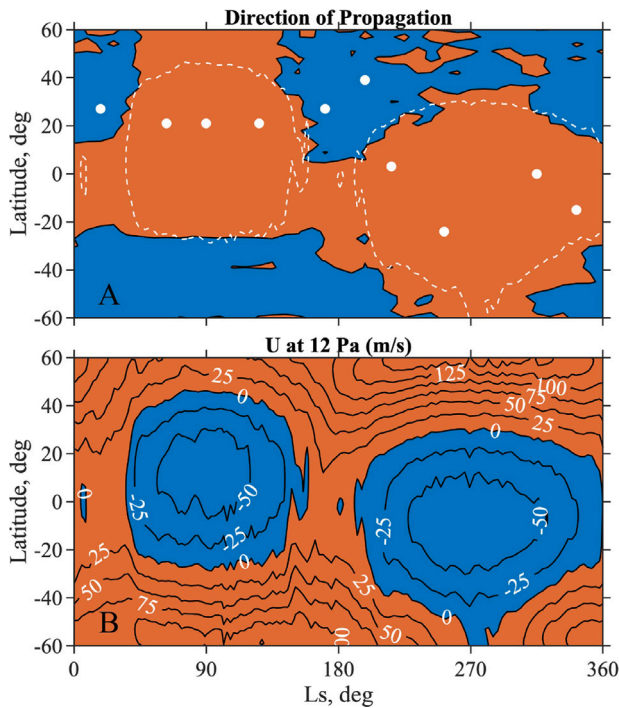


Fig. 16. (A) The direction of wave propagation, as inferred from the tilt of the wavefronts in the MCS measurements. Orange denotes eastward and blue denotes westward. White circles mark the latitude and season of the MCS measurements in Figs. 4, 7 and 17. (B) The mean zonal wind speed at the 12-Pa pressure level in the MGCM simulation. The contour interval is 25 m s^{-1} . Shading indicates the wind direction, orange for eastward and blue for westward. The zero contour in B is shown by the dashed white line in A. (For interpretation of the references to color in this figure legend, the reader is referred to the web version of this article.)

contours at $\pm 25\%$ and $\pm 40\%$ of the peak amplitude and the median slope is essentially the same.

The median slope of the wavefronts — and hence, the direction of propagation relative to the surface — follows an orderly seasonal cycle, as shown in Fig. 16A. Eastward-traveling waves are observed by MCS at low latitudes (20°N – 20°S) throughout the year. At midlatitudes (20° – 60°) in both hemispheres, the waves generally propagate eastward near the summer solstice and westward near the winter solstice. A comparison with the mean zonal wind field in the MGCM simulation (Fig. 16B) shows that u_p and U generally have opposite signs. Eastward-traveling waves predominate at seasons and latitudes where U is westward, and westward-traveling waves predominate where U is eastward.

We validated the results in Fig. 16A through comparisons with the longitude-height cross sections in Figs. 4, 7 and 17. This set of observations is distributed in L_s and latitude, as shown in Fig. 16A; it includes examples of both eastward- and westward-tilting waves. In each case, the median slope is consistent with the tilt of the wavefronts. Figs. 7 and 17 also illustrate that the response to forcing by a particular surface feature depends on the seasonal configuration of the zonal winds. Sources in the northern tropics produce deep, eastward-tilting waves at $L_s = 63^\circ$ (Fig. 7B) and 126° (Fig. 17A); this is the northern-summer-solstice configuration of the zonal wind field shown in Fig. 13B and 13C. The same sources produce deep, westward-tilting waves at $L_s = 18^\circ$ (Fig. 7A) and 171° (Fig. 17B); this is the equinox configuration of the zonal wind field shown in Fig. 13A and 13D.

5. Summary and discussion

This paper reports results from a detailed investigation of a type of wave first identified by Wilson and Hinson (2021). We determined

basic properties of the waves through analysis of MCS temperature profiles. We then used a simulation by the NASA Ames MGCM to explore aspects of wave behavior that cannot be measured directly. We have confidence in the accuracy of the simulation because of the many similarities between the simulated waves and the ones observed by MCS. The model performs well in comparisons of longitude-height cross sections (Fig. 7A–C and Fig. 8A–C), longitude-latitude cross sections (Fig. 7E and Fig. 15C), and latitude-pressure cross sections (Fig. 9A and 9B).

Elysium Mons and the pedestal on which it stands are well separated from other wave sources (Fig. 12), which makes the atmospheric dynamics easier to interpret. The MGCM simulation identified the source of the wave — an upward surge of air caused by convergence of upslope flow onto the pedestal (Fig. 11). This sort of forcing is present only at local times of about 13–18 h (Fig. 10), which results in a wave whose amplitude varies strongly with time of day. DWPs at other locations exhibit the same behavior (Fig. 8G–I). The presence of wave packets rather than steady oscillations is also apparent in the MCS observations (Fig. 7D–I).

In observations at fixed local time, $m \approx 15$ and the zonal wavelength is about 1400 km (Section 4.1). The DWPs are not stationary; their zonal phase speed has a magnitude of about 25 m s^{-1} , and it can be eastward or westward (Fig. 8G–I). Waves with this combination of m and zonal phase speed are roughly semidiurnal ($\sigma = \pm 2$). Thus, the difference between m and the true zonal wavenumber s is relatively small, because $s = m - \sigma$ (Section 3), and $m \gg |\sigma|$ for the waves considered here. We therefore adopt 1400 km as a generic value for the true zonal wavelength of the DWPs. The vertical wavelength is about 40 km (Figs. 4, 7 and 17).

The DWPs are localized in longitude and appear primarily in the tropics. Several wave sources are apparent in the MCS observations: Elysium Mons, Olympus Mons, the Tharsis Montes, and the rim of Isidis Planitia (Fig. 7). These and other sources were identified by the MGCM through the presence of convergence zones, which form in connection with upslope flows produced by steep topography (Fig. 12). Some convergence zones are strikingly long and narrow, such as the ones aligned with the rim of Isidis Planitia, Valles Marineris, and the Tharsis Montes. The intensity of the convergence zone associated with a particular surface feature generally varies with season.

The waves follow a well-defined annual cycle with little year-to-year variability. The predominant direction of propagation changes with season (Fig. 16), a consequence of the seasonal evolution of the diurnal-mean zonal winds (Fig. 13) and wave filtering by critical levels. In addition, amplitudes at most locations are larger in summer than winter, owing to the seasonal evolution of the underlying convergence zones (Fig. 12). The north-south asymmetry of wave structure at both solstices is also apparent in MCS off-nadir radiance measurements (Wilson and Hinson, 2021).

In addition to generating atmospheric waves, topographic circulations have other important effects. Tyler and Barnes (2015) showed that the circulation induced by an idealized crater not only reduces the depth of the daytime convective boundary layer (CBL) within the crater but also produces large diurnal variations of surface pressure on the crater floor. The same effects are apparent in a simulation by the OSU MMM of the far more complex circulation in and around Gale Crater (Tyler and Barnes, 2013). The diurnal cycle of upslope/downslope winds at the rim of Isidis Planitia causes similar anomalies in both surface pressure (Wilson et al., 2017) and CBL depth (Hinson et al., 2019) within the Isidis basin. From the results reported here it is now clear that slope-flow circulations also generate a distinct type of atmospheric wave.

We did not consider wave dissipation and its effect on the global circulation; this would be an interesting topic for future work. In this regard, it is important to characterize waves excited by convergence zones that were not resolved by our C48 simulation. Their cumulative effect could be assessed in the context of a C768 simulation like

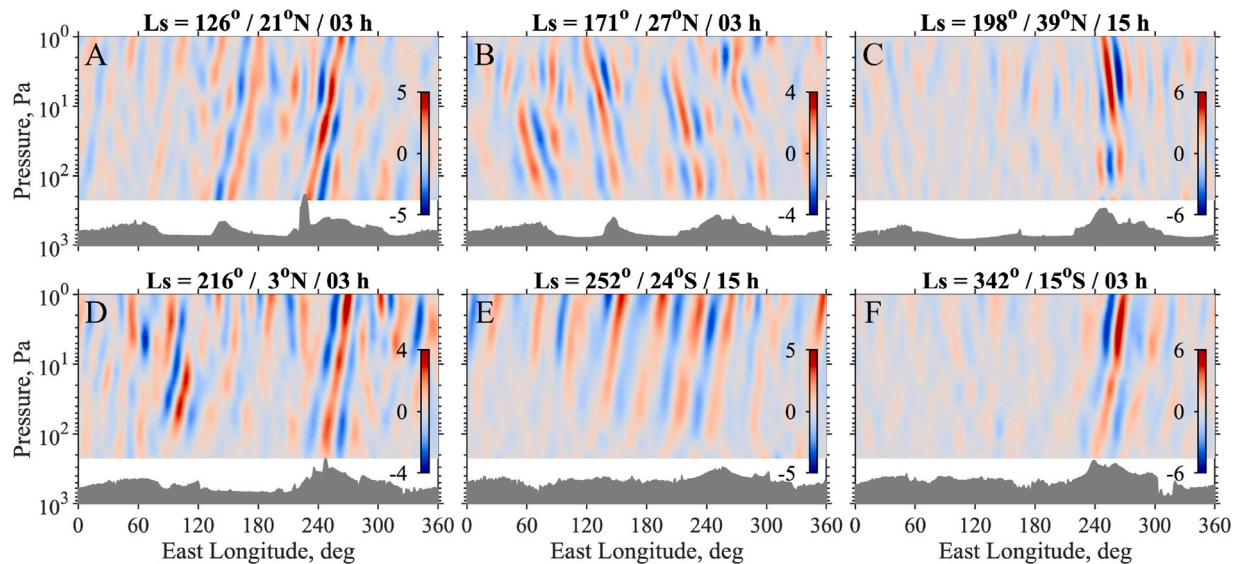


Fig. 17. Longitude-height cross sections of wave-induced temperature variations observed by MCS. The units on the color bars are K. The season, latitude, and local time are indicated in the title to each panel. (For interpretation of the references to color in this figure legend, the reader is referred to the web version of this article.)

the one described by Wilson et al. (2017). The results might provide new constraints on parameterizations used by MGCMs to represent momentum transport by sub-grid-scale waves (Medvedev et al., 2011; Neary and Daerden, 2018).

Declaration of competing interest

The authors declare that they have no known competing financial interests or personal relationships that could have appeared to influence the work reported in this paper.

Data availability

Data will be made available on request.

Acknowledgments

This research was made possible by financial support from grant 80NSSC19K0015 of the NASA Mars Data Analysis Program.

Appendix A. Supplementary data

Supplementary material related to this article can be found online at <https://doi.org/10.1016/j.icarus.2022.115420>.

Two data products are available; both are animations of results from the MGCM simulation. The first one shows longitude-height cross sections in the same format as Fig. 10, with 24 frames at 1-h intervals of local time. The second one shows longitude-latitude cross sections in the same format as Fig. 15, again with 24 frames at 1-h intervals of local time. See the captions to Figs. 10 and 15 for further information. Both MP4s are most effective when viewed as a loop.

References

- Ando, H., Imamura, T., Tsuda, T., 2012. Vertical wavenumber spectra of gravity waves in the Martian atmosphere obtained from Mars global surveyor radio occultation data. *J. Atmos. Sci.* 69, 2906–2912. <http://dx.doi.org/10.1175/JAS-D-11-0339.1>.
- Andrews, D.G., Holton, J.R., Leovy, C.B., 1987. *Middle Atmosphere Dynamics*. Elsevier, New York.
- Barnes, J.R., Haberle, R.M., Wilson, R.J., Lewis, S.R., Murphy, J.R., Read, P.L., 2017. The global circulation. In: Haberle, R.M., Clancy, R.T., Forget, F., Smith, M.D., Zurek, R.W. (Eds.), *The Atmosphere and Climate of Mars*. Cambridge University Press, pp. 229–294. <http://dx.doi.org/10.1017/9781139060172.009>.
- Bertrand, T., Wilson, R.J., Kahre, M.A., Urata, R., Kling, A., 2020. Simulation of the 2018 global dust storm on Mars Using the NASA Ames Mars GCM: A multitracer approach. *J. Geophys. Res. (Planets)* 125, e06122. <http://dx.doi.org/10.1029/2019JE006122>.
- Clancy, R.T., Sandor, B.J., Wolff, M.J., Christensen, P.R., Smith, M.D., Pearl, J.C., Conrath, B.J., Wilson, R.J., 2000. An intercomparison of ground-based millimeter, MGS TES, and viking atmospheric temperature measurements: Seasonal and interannual variability of temperatures and dust loading in the global Mars atmosphere. *J. Geophys. Res.* 105, 9553–9572. <http://dx.doi.org/10.1029/1999JE001089>.
- Creasey, J.E., Forbes, J.M., Hinson, D.P., 2006. Global and seasonal distribution of gravity wave activity in Mars' lower atmosphere derived from MGS radio occultation data. *Geophys. Res. Lett.* 33, L01803. <http://dx.doi.org/10.1029/2005GL024037>.
- Fan, S., Forget, F., Smith, M.D., Guerlet, S., Badri, K.M., Atwood, S.A., Young, R.M.B., Edwards, C.S., Christensen, P.R., Deighan, J., Al Matroushi, H.R., Bierjon, A., Liu, J., Millour, E., 2022a. Migrating thermal tides in the Martian atmosphere during aphelion season observed by EMM/EMIRS. *Geophys. Res. Lett.* 49, <http://dx.doi.org/10.1029/2022GL099494>, e2022GL099494.
- Fan, S., Guerlet, S., Forget, F., Bierjon, A., Millour, E., Ignatiev, N., Shakun, A., Grigoriev, A., Trokhimovskiy, A., Montmessin, F., Korabely, O., 2022b. Thermal tides in the Martian atmosphere near northern summer solstice observed by ACS/TIRVIM onboard TGO. *Geophys. Res. Lett.* 49, e97130. <http://dx.doi.org/10.1029/2021GL097130>.
- Forbes, J.M., Zhang, X., Forget, F., Millour, E., Kleinböhl, A., 2020. Solar tides in the middle and upper atmosphere of Mars. *J. Geophys. Res. (Space Physics)* 125, e28140. <http://dx.doi.org/10.1029/2020JA028140>.
- Fritts, D.C., Alexander, M.J., 2003. Gravity wave dynamics and effects in the middle atmosphere. *Rev. Geophys.* 41, 1003. <http://dx.doi.org/10.1029/2001RG000106>.
- Guzewich, S.D., Talaat, E.R., Waugh, D.W., 2012. Observations of planetary waves and nonmigrating tides by the Mars climate sounder. *J. Geophys. Res. (Planets)* 117, E03010. <http://dx.doi.org/10.1029/2011JE003924>.
- Haberle, R.M., Kahre, M.A., Hollingsworth, J.L., Montmessin, F., Wilson, R.J., Urata, R.A., Brecht, A.S., Wolff, M.J., Kling, A.M., Schaeffer, J.R., 2019. Documentation of the NASA/Ames legacy Mars global climate model: Simulations of the present seasonal water cycle. *Icarus* 333, <http://dx.doi.org/10.1016/j.icarus.2019.03.026>.
- Heavens, N.G., Kass, D.M., Kleinböhl, A., Schofield, J.T., 2020. A multiannual record of gravity wave activity in Mars's lower atmosphere from on-planet observations by the Mars climate sounder. *Icarus* 341, 113630. <http://dx.doi.org/10.1016/j.icarus.2020.113630>.
- Heavens, N.G., Pankine, A., Battalio, J.M., Wright, C., 2022a. The horizontal wavelength spectrum of gravity wave activity in Mars's lower atmosphere: The perspective from MGS-TES nadir observations. *Planet. Sci. J.* 3, 228. <http://dx.doi.org/10.3847/PSJ/ac8d62>.
- Heavens, N.G., Pankine, A., Battalio, J.M., Wright, C., Kass, D.M., Kleinböhl, A., Piqueux, S., Schofield, J.T., 2022b. Mars climate sounder observations of gravity-wave activity throughout Mars's lower atmosphere. *Planet. Sci. J.* 3, 57. <http://dx.doi.org/10.3847/PSJ/ac51ce>.
- Hinson, D.P., Pätzold, M., Wilson, R.J., Häusler, B., Tellmann, S., Tyler, G.L., 2008. Radio occultation measurements and MGCM simulations of Kelvin waves on Mars. *Icarus* 193, 125–138. <http://dx.doi.org/10.1016/j.icarus.2007.09.009>.

- Hinson, D.P., Tyler, D., Lewis, S.R., Pätzold, M., Tellmann, S., Häusler, B., Tyler, G.L., 2019. The Martian daytime convective boundary layer: Results from radio occultation measurements and a mesoscale model. *Icarus* 326, 105–122. <http://dx.doi.org/10.1016/j.icarus.2019.02.028>.
- Kleinböhl, A., Schofield, J.T., Abdou, W.A., Irwin, P.G.J., de Kok, R.J., 2011. A single-scattering approximation for infrared radiative transfer in limb geometry in the Martian atmosphere. *J. Quant. Spectrosc. Radiat. Transfer* 112, 1568–1580. <http://dx.doi.org/10.1016/j.jqsrt.2011.03.006>.
- Kleinböhl, A., Schofield, J.T., Abdou, W.A., Backus, C.R., Sen, B., Shirley, J.H., Lawson, W.G., Richardson, M.L., Taylor, F.W., Teanby, N.A., McCleese, D.J., 2009. Mars climate sounder limb profile retrieval of atmospheric temperature, pressure, and dust and water ice opacity. *J. Geophys. Res. (Planets)* 114, E10006. <http://dx.doi.org/10.1029/2009JE003358>.
- Kleinböhl, A., Wilson, R.J., Kass, D., Schofield, J.T., McCleese, D.J., 2013. The semidiurnal tide in the middle atmosphere of Mars. *Geophys. Res. Lett.* 40, 1952–1959. <http://dx.doi.org/10.1002/grl.50497>.
- Lewis, S.R., Read, P.L., 2003. Equatorial jets in the dusty Martian atmosphere. *J. Geophys. Res. (Planets)* 108, 5034. <http://dx.doi.org/10.1029/2002JE001933>.
- McCleese, D.J., Schofield, J.T., Taylor, F.W., Calcutt, S.B., Foote, M.C., Kass, D.M., Leovy, C.B., Paige, D.A., Read, P.L., Zurek, R.W., 2007. Mars climate sounder: An investigation of thermal and water vapor structure, dust and condensate distributions in the atmosphere, and energy balance of the polar regions. *J. Geophys. Res. (Planets)* 112(E05), E05S06. <http://dx.doi.org/10.1029/2006JE002790>.
- Medvedev, A.S., Yigit, E., Hartogh, P., Becker, E., 2011. Influence of gravity waves on the Martian atmosphere: General circulation modeling. *J. Geophys. Res.: Planets* 116, E10004. <http://dx.doi.org/10.1029/2011JE003848>.
- Montabone, L., Forget, F., Millour, E., Wilson, R.J., Lewis, S.R., Cantor, B., Kass, D., Kleinböhl, A., Lemmon, M.T., Smith, M.D., Wolff, M.J., 2015. Eight-year climatology of dust optical depth on Mars. *Icarus* 251, 65–95. <http://dx.doi.org/10.1016/j.icarus.2014.12.034>.
- Neary, L., Daerden, F., 2018. The GEM-Mars general circulation model for Mars: Description and evaluation. *Icarus* 300, 458–476. <http://dx.doi.org/10.1016/j.icarus.2017.09.028>.
- Sánchez-Lavega, A., Rio-Gaztelurrutia, T.d., Hueso, R., Juárez, M.d.I.T., Martínez, G.M., Harri, A.-M., Genzer, M., Hietä, M., Polkko, J., Rodríguez-Manfredi, J.A., Lemmon, M.T., Pla-García, J., Toledo, D., Vicente-Retortillo, A., Viúdez-Moreiras, D., Munguira, A., Tamppari, L.K., Newman, C., Gómez-Elvira, J., Guzewich, S., Bertrand, T., Apéstigue, V., Arruego, I., Wolff, M., Banfield, D., Jaakonaho, I., Mäkinen, T., 2023. Mars 2020 perseverance rover studies of the Martian atmosphere over Jezero from pressure measurements. *J. Geophys. Res.: Planets* XXX, <http://dx.doi.org/10.1029/2022JE007480>, e2022JE007480, (in press).
- Smith, D.E., Zuber, M.T., Frey, H.V., Garvin, J.B., Head, J.W., Muhleman, D.O., Pettengill, G.H., Phillips, R.J., Solomon, S.C., Zwally, H.J., Banerdt, W.B., Duxbury, T.C., Golombek, M.P., Lemoine, F.G., Neumann, G.A., Rowlands, D.D., Aharonson, O., Ford, P.G., Ivanov, A.B., Johnson, C.L., McGovern, P.J., Abshire, J.B., Afzal, R.S., Sun, X., 2001. Mars orbiter laser altimeter: Experiment summary after the first year of global mapping of Mars. *J. Geophys. Res.* 106, 23,689–23,722. <http://dx.doi.org/10.1029/2000JE001364>.
- Starichenko, E.D., Belyaev, D.A., Medvedev, A.S., Fedorova, A.A., Korablev, O.I., Trokhimovskiy, A., Yigit, E., Alday, J., Montmessin, F., Hartogh, P., 2021. Gravity wave activity in the Martian atmosphere at altitudes 20–160 km from ACS/TGO occultation measurements. *J. Geophys. Res. (Planets)* 126, e06899. <http://dx.doi.org/10.1029/2021JE006899>.
- Tellmann, S., Pätzold, M., Häusler, B., Hinson, D.P., Tyler, G.L., 2013. The structure of Mars lower atmosphere from Mars express radio science (MaRS) occultation measurements. *J. Geophys. Res. (Planets)* 118, 306–320. <http://dx.doi.org/10.1002/jgre.20058>.
- Tyler, D., Barnes, J.R., 2013. Mesoscale modeling of the circulation in the Gale Crater Region: An investigation into the complex forcing of convective boundary layer depths. *Int. J. Mars Sci. Explor.* 8, 58–77. <http://dx.doi.org/10.1555/mars.2013.0003>.
- Tyler, D., Barnes, J.R., 2015. Convergent crater circulations on Mars: Influence on the surface pressure cycle and the depth of the convective boundary layer. *Geophys. Res. Lett.* 42, 7343–7350. <http://dx.doi.org/10.1002/2015GL064957>.
- Wilson, R.J., 2000. Evidence for diurnal period Kelvin waves in the Martian atmosphere from Mars global surveyor TES data. *Geophys. Res. Lett.* 27, 3889–3892. <http://dx.doi.org/10.1029/2000GL012028>.
- Wilson, R.J., Guzewich, S.D., 2014. Influence of water ice clouds on nighttime tropical temperature structure as seen by the Mars climate sounder. *Geophys. Res. Lett.* 41, 3375–3381. <http://dx.doi.org/10.1002/2014GL060086>.
- Wilson, R.J., Hamilton, K., 1996. Comprehensive model simulation of thermal tides in the Martian atmosphere. *J. Atmos. Sci.* 53, 1290–1326. [http://dx.doi.org/10.1175/1520-0469\(1996\)053<1290:CMSOTT>2.0.CO;2](http://dx.doi.org/10.1175/1520-0469(1996)053<1290:CMSOTT>2.0.CO;2).
- Wilson, R., Hinson, D., 2021. Topographically localized non-migrating tides in the Mars tropical atmosphere. In: AGU Fall Meeting. P35F-2194, URL <https://agu2021fallmeeting-agu.ipostersessions.com/default.aspx?s=90-FC-ED-B1-1A-F1-1F-8F-B8-81-B7-4E-15-11-D8-83>.
- Wilson, R.J., Murphy, J.M., Tyler, D., 2017. Assessing atmospheric thermal forcing from surface pressure data: Separating thermal tides and local topographic influence. In: Sixth International Workshop on the Mars Atmosphere: Modelling and Observations. URL http://www-mars.lmd.jussieu.fr/granada2017/program_granada2017.htm.
- Wright, C.J., 2012. A one-year seasonal analysis of martian gravity waves using MCS data. *Icarus* 219, 274–282. <http://dx.doi.org/10.1016/j.icarus.2012.03.004>.
- Wu, Z., Li, T., Dou, X., 2015. Seasonal variation of Martian middle atmosphere tides observed by the Mars climate sounder. *J. Geophys. Res. (Planets)* 120 (12), 2206–2223. <http://dx.doi.org/10.1002/2015JE004922>.
- Wu, Z., Li, T., Dou, X., 2017. What causes seasonal variation of migrating diurnal tide observed by the Mars climate sounder? *J. Geophys. Res. (Planets)* 122, 1227–1242. <http://dx.doi.org/10.1002/2017JE005277>.
- Zurek, R.W., 1988. Free and forced modes in the Martian atmosphere. *J. Geophys. Res.* 93, 9452–9462. <http://dx.doi.org/10.1029/JD093iD08p09452>.
- Zurek, R.W., Barnes, J.R., Haberle, R.M., Pollack, J.B., Tillman, J.E., Leovy, C.B., 1992. Dynamics of the atmosphere of Mars. In: Kieffer, H.H., Jakosky, B.M., Snyder, C.W., Matthews, M.S. (Eds.), *Mars. Univ. of Arizona Press, Tucson*, pp. 835–933.
- Zurek, R.W., Smrekar, S.E., 2007. An overview of the Mars reconnaissance orbiter (MRO) science mission. *J. Geophys. Res. (Planets)* 112(E05), E05S01. <http://dx.doi.org/10.1029/2006JE002701>.